Geochemistry Geophysics Geosystems G3

Published by AGU and the Geochemical Society

Article
Volume 12, Number 12
13 December 2011
Q12009, doi:10.1029/2011GC003693
ISSN: 1525-2027

Does sea level influence mid-ocean ridge magmatism on Milankovitch timescales?

David C. Lund
Department of Earth and Environmental Sciences, University of Michigan, Ann Arbor, Michigan 48109, USA (dclund@umich.edu)

Paul D. Asimow
Division of Geological and Planetary Sciences, California Institute of Technology, Pasadena, California 91125, USA

[1] Magma production at mid-ocean ridges is driven by seafloor spreading and decompression melting of the upper mantle. In the special case of Iceland, mantle melting may have been amplified by ice sheet retreat during the last deglaciation, yielding anomalously high rates of subaerial volcanism. For the remainder of the global mid-ocean ridge system, the ocean may play an analogous role, with lowering of sea level during glacial maxima producing greater magma flux to ridge crests. Here we show that the mantle decompression rate associated with changes in sea level is a substantial fraction of that from plate spreading. Modeled peaks in magma flux occur after sea level drops rapidly, including the Marine Isotope Stage (MIS) 5/4 and 3/2 transitions. The minimum in simulated flux occurs during the mid-Holocene, due to the rapid sea level rise at the MIS 2/1 boundary. The model results are highly sensitive to melt migration rate; rates of ~1 m/yr produce small signals, while those >5 m/yr yield substantial anomalies. In the latter case, sea level-driven magma flux varies by 15–100% relative to the long-term average, with the largest effect occurring at slow-spreading ridges. We suggest that sedimentary time series of hydrothermal particle flux, oceanic Os isotopic ratio, and oceanic radiocarbon may serve as proxies for magma-flux variations at mid-ocean ridges. Although well-dated records are rare, preliminary data from the Pacific and Atlantic suggest hydrothermal metal flux was elevated during MIS 2 and 4, broadly consistent with our modeling results.

Components: 14,300 words, 15 figures, 1 table.

Keywords: Milankovitch; magmatism; sea level.

Index Terms: 3035 Marine Geology and Geophysics: Midocean ridge processes.

Received 10 May 2011; **Revised** 12 October 2011; **Accepted** 13 October 2011; **Published** 13 December 2011.

Lund, D. C., and P. D. Asimow (2011), Does sea level influence mid-ocean ridge magmatism on Milankovitch timescales?, *Geochem. Geophys. Geosyst.*, *12*, Q12009, doi:10.1029/2011GC003693.

1. Introduction and Background

[2] It is well documented that Iceland experienced a pulse of elevated volcanism immediately following the last deglaciation [*Maclennan et al.*, 2002]. Subaerial volcanism apparently increased at other high-latitude locations as well [*Huybers and Langmuir*, 2009]. In the Iceland case, decreasing overburden load from ice sheet retreat reduced pressure in the underlying mantle, enhancing melt production and magma supply to the surface [*Jull and McKenzie*,

1996]. Here we focus on the effect of sea level on mantle melting at mid-ocean ridges. Changes in load due to variable glacioeustatic sea level are smaller in amplitude than the local impact of deglaciation in Iceland, but they simultaneously affect all the world's mid-ocean ridges and so may have significant global impacts. We model the effect of sea level on melting at mid-ocean ridges and find that glacial-interglacial sea level forcing may alter magma delivery to ridges by ≥30%.

[3] As a means to evaluate our hypothesis, we discuss proxies of hydrothermal activity, including concentrations of metals in hydrothermal sediments, the oceanic Os isotopic ratio, and the radiocarbon content of seawater. The existing data are inconclusive, though isolated records from the Atlantic and Pacific suggest that hydrothermal activity during the last glacial cycle may have varied in phase with the predictions of our melting model. The aim of this paper is not to conclusively show that sea level forces mid-ocean ridge magmatism on Milankovitch timescales, but instead to raise the possibility. Indeed, such an unusual hypothesis will require an unusual amount of supporting data. As we discuss below, these data do not yet exist, but there are some promising leads.

1.1. Sea Level Driven Decompression Melting

[4] To determine the influence of sea level on mantle melting, we first evaluate the rates of pressure change that sea level and plate spreading impose on material points in a melting regime. In a constant-viscosity analytical corner flow solution for passive, plate-driven flow [*Batchelor*, 1967], the change in pressure per time (dP/dt) directly beneath the axis of a mid-ocean ridge is given by

$$\frac{dP}{dt} = g\,(k\rho_{lith}v_{lith} + \rho_{water}v_{water}), \quad (1)$$

where g is the acceleration due to gravity. The first term, representing lithostatic unloading due to plate spreading, depends on mantle density (ρ_{lith}; 3300 kg/m^3), half-spreading rate (v_{lith}; in m/yr), and a geometric factor k, which modifies the linear scaling between upwelling rate and half spreading rate and approximates the effect of a thickening lithosphere with distance from the ridge [*Spiegelman and McKenzie*, 1987]:

$$k = \frac{2\sin^2\alpha - 2}{\pi - 2\alpha - \sin 2\alpha}, \quad (2)$$

where α is the angle measured downward from the seafloor of the line along which strictly horizontal flow is imposed. Most studies since *Spiegelman and McKenzie* [1987] have neglected this lithospheric wedge, but it affects our results so despite the added complexity we examined the sensitivity of our results to this parameter.

[5] The sea level term depends on seawater density (ρ_{water}; 1030 kg/m^3) and the rate of sea level change (v_{water}; in m/yr). For a rate of sea level change of ±10 mm/yr, $(dP/dt)_{water}$ ~±100 Pa/yr. By comparison, rates of mantle unloading yield $(dP/dt)_{lith}$ values of −200 to −1550 Pa/yr when the effect of lithospheric thickening is ignored ($\alpha = 0$), or −510 to 2050 Pa/yr using the wedge angle formalism of *Spiegelman and McKenzie* [1987] to approximate lithospheric thickening ($\alpha \neq 0$) (Table 1).

[6] The effect of sea level on decompression melting should be largest at slow spreading ridges like the Mid-Atlantic Ridge (MAR), where it is up to 50% of mantle unloading term (Table 1). The effect is smallest at fast ridges like the East Pacific Rise (EPR), where it is approximately 5% of the mantle unloading term. The effect of the lithosphere on concentrating the upwelling flow into a narrower, faster channel is significant, especially at slow spreading rate (Table 1), but even so this conservative estimate indicates that sea level variations may create a substantial perturbation to the unloading rates experienced by upwelling mantle. Off-axis points in the melting regime experience lower vertical velocities, so calculations based on the vertical velocity directly below the axis in Table 1 yield a minimum estimate of the relative significance of the sea level term.

[7] We note that a large component of active, buoyancy-driven flow can concentrate upwelling in to an even faster, narrower zone with larger decompression rates and correspondingly smaller sea level effects. However, this type of flow, considered in a number of early papers [*Scott and Stevenson*, 1989; *Turcotte and Morgan*, 1992; *Forsyth*, 1992], has fallen out of favor in recent decades due to seismic, geochemical, and rheological arguments for dominantly passive, plate-driven flow [*Forsyth et al.*, 1998; *Hung et al.*, 2000; *Spiegelman*, 1996; *Braun et al.*, 2000]. Hence in this paper we model only strictly passive plate-driven mantle flow fields.

1.2. Records of Sea Level

[8] Many coral species grow near the sea surface and therefore their stratigraphic position on terraces

Table 1. Relative Effect of Sea Level Pressure Change at Slow, Intermediate, and Fast Ridges

	$\alpha = 0$			$\alpha \neq 0$	
Half-Spreading Rate (mm/yr)	$(dP/dt)_{lith}$ (Pa/yr)	Sea Level Effect	α (°)	$(dP/dt)_{lith}$ (Pa/yr)	Sea Level Effect
10 (e.g., Northern MAR)	−206	49%	41	−510	20%
30 (e.g., Galapagos SC)	−618	16%	24	−1039	10%
75 (e.g., Southern EPR)	−1546	6%	13	−2050	5%

with known uplift rates can be used to estimate sea level in the geologic past. For more than 20 years, it has been known that sea level rose by ~120 m from the Last Glacial Maximum (LGM) to the early Holocene [*Bard et al.*, 1990a; *Fairbanks et al.*, 2005]. Recent compilations of U-series dated corals by *Cutler et al.* [2003] (hereafter C03) and *Thompson and Goldstein* [2006] (hereafter TG06) provide a more complete picture of sea level prior to the LGM (Figure 1). C03 relied primarily on coral samples

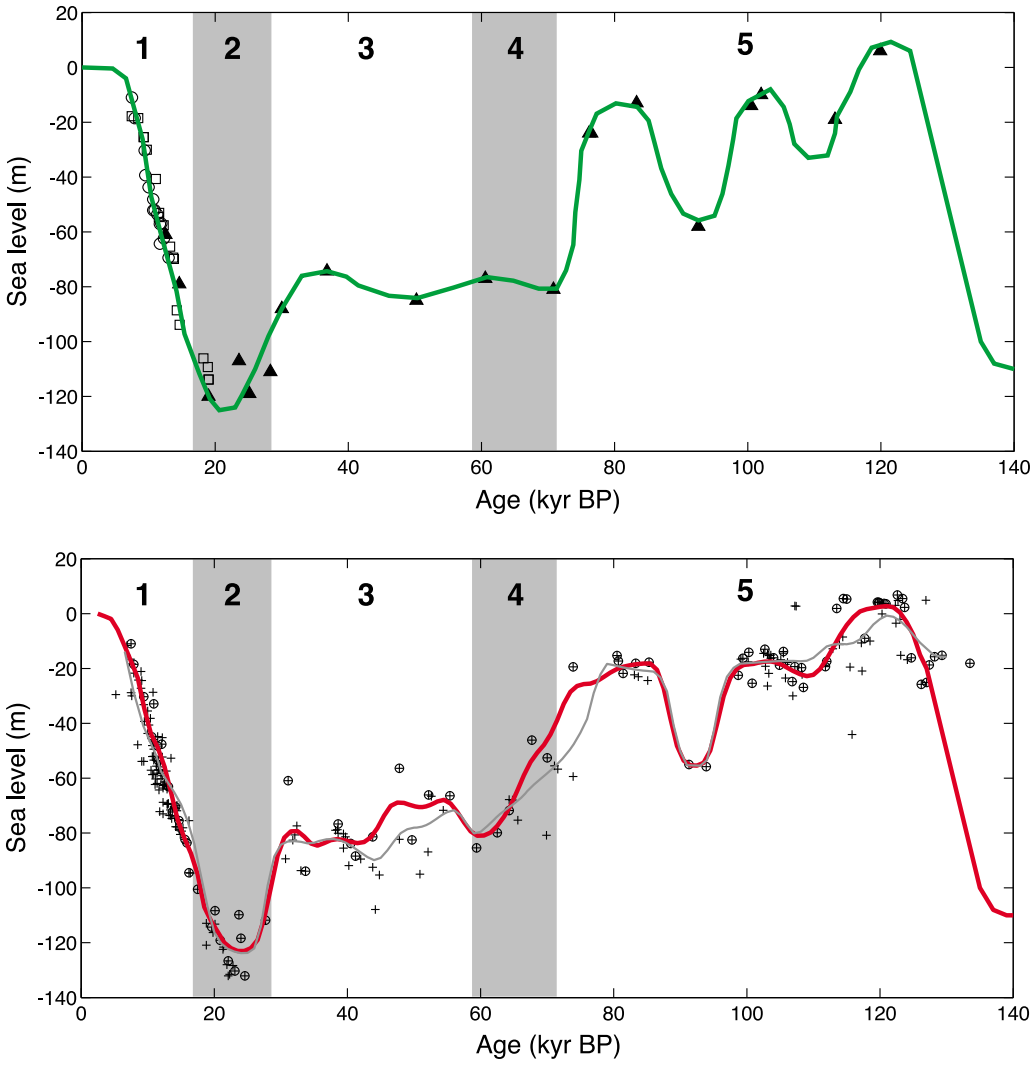

Figure 1. Sea level curves for the last 140,000 years. (top) A manual interpolation of coral data from *Cutler et al.* [2003] (triangles), *Bard et al.* [1990b] (squares) and *Edwards et al.* [1993] (circles). (bottom) *Thompson and Goldstein* [2006] coral results (pluses) fitted by a Gaussian smoothing of all results (light gray curve) and a Gaussian smoothing (thick red curve) of only the shallowest data from each time interval (circled pluses). For both panels, the sea level curves before 120,000 yr BP are based on the modeling work of *Bintanja et al.* [2005]. Approximate time intervals of Marine Isotope Stages 1, 2, 3, 4, and 5 are noted [*Lisiecki and Raymo*, 2005].

that met two strict criteria: 1) an initial δ^{234}U similar to the modern ocean, and 2) concordant ages between the ^{238}U-^{230}Th and ^{235}U-^{231}Pa dating techniques. These filters excluded most of the available published data but nonetheless a surprising picture emerged (Figure 1, top). The lowering of sea level between Marine Isotope Stages (MIS) 5 and 2 was not a slow, monotonic process, but rather it occurred in two key steps, first at the MIS 5/4 boundary and then at the MIS 3/2 boundary. In each case, sea level fell quickly, at a rate of 5–10 m/kyr. Sea level unloading during ice sheet growth can apparently be comparable in magnitude to sea level loading during deglaciation.

[9] The results of C03 are supported by the more recent compilation of TG06 (Figure 1, bottom). In TG06, coral U/Th data from the literature were corrected assuming that initial δ^{234}U values were similar to δ^{234}U in the modern ocean and that corals from the same terrace could be used to correct for open system behavior. The amplitude and rate of sea level increase during the last deglaciation in C03 and TG06 are similar. However, TG06 estimate a 40–60 m decrease in sea level at the MIS 5c/5b, MIS 5/4, and MIS 3/2 boundaries. Here again the rates of sea level drop are rapid, ranging from 5 to 8 m/kyr. The rate during the MIS 5/4 transition is slower than in C03, while the rate at the MIS 3/2 boundary is faster. A more recent compilation suggests the rate of sea level change at the MIS 3/2 transition was 7 m/kyr [*Clark et al.*, 2009]. Despite the differences between the sea level reconstructions, the overall pattern of change during the last 120 kyr is similar, with comparable rates of sea level rise and fall.

2. Methods

2.1. Model Description

[10] Our model of melt production uses the average upper mantle source composition of *Workman and Hart* [2005] with 150 ppm H_2O, the pHMELTS melting model [*Asimow et al.*, 2004; *Ghiorso et al.*, 2002] and analytical corner flow velocities. We adopt the corner-flow solution from *Spiegelman and McKenzie* [1987] that allows the wedge-angle parameter α to account for possible effects of lithospheric thickening, although most authors over the last 20 years have ignored this effect. Our two-dimensional model domain spans 125 km on either side of the ridge axis and is 125 km deep (Figure 2).

[11] We used pHMELTS calculations of near-fractional decompression melting (residual porosity 0.01%) to generate a look-up table of melt productivity (mass of melt per unit pressure decrease and per unit original source mass) versus potential temperature [*Asimow et al.*, 2004; *McKenzie and Bickle*, 1988] and pressure. This function accounts for depletion of the source by prior melting along a streamline from solidus to pressure of interest. Melt productivity predicted by pHMELTS features very low productivity initial volatile-driven melting, acceleration near the dry solidus, further acceleration to a sharp maximum just before clinopyroxene exhaustion at ~20% melting, and low (but nonzero) productivity of harzburgite [*Asimow et al.*, 1997, 2001, 2004]. Here, for the cases with wedge angle $\alpha = 0$, we use a potential temperature of 1344°C, which (for the selected source composition) gives a damp solidus intersection depth of 2.8 GPa (85 km), onset of major silicate melting at 1.5 GPa (49 km), and steady state crustal thickness of 6.3 km. In cases with nonzero α, we lower the potential temperature (by up to 24°C) in order to keep the steady state crustal thickness the same for all cases.

[12] Constant viscosity analytical corner flow [*Batchelor*, 1967; *Spiegelman and McKenzie*, 1987] and the half-spreading rate provide a vertical component of velocity at each point in a passive, plate-driven mantle flow, converted to tectonic decompression rate using constant mantle density (3300 kg/m^3). To this steady decompression rate, we add a time-dependent sea level-driven term obtained from the density of water multiplied by the derivative of the sea level history of either C03 or TG06. We assume that the pressure signal from seawater loading is felt instantaneously and without attenuation throughout the melting regime. This is probably a reasonable assumption. The driving force is uniformly distributed horizontally over the entire ocean, a much larger scale than the melting regime (except for ridges close to land, e.g., Iceland or the Gulf of California), which greatly simplifies this calculation compared to the axisymmetric solution for a finite scale ice-load used by *Jull and McKenzie* [1996]. The load propagates as a compressional wave with characteristics that depend on the rheology of the crust and mantle. The wavelength is long enough that flexural support by the lithosphere can be neglected. The dominant elastic component moves down at elastic velocities of several km/s, or effectively instantaneously in a model with 1000 year time steps. There may also be a viscous component, since pressure changes causing melting or freezing are accommodated by bulk deformation (compaction/decompaction) of partially molten mantle, but this signal propagates as porosity

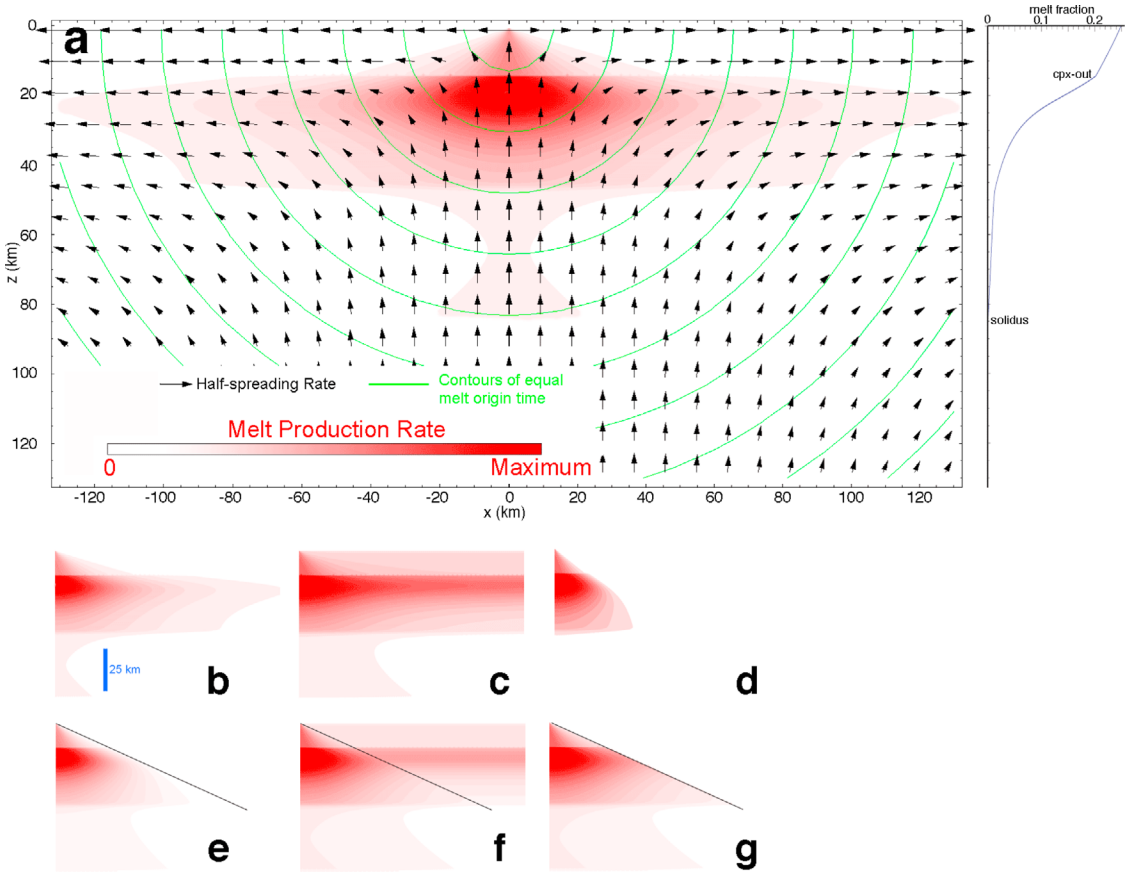

Figure 2. (a) Schematic depiction of the mantle flow, melt production and melt migration model. Black arrows show the solid mantle flow field derived from analytical corner flow solution, in this case with no lithospheric wedge. Arrow length is proportional to velocity. Melting at any point is a function of the melt productivity and the combined effect of lithostatic and hydrostatic pressure variability. The steady state melt production field (that is, no sea level change) is contoured in shades of red. For a half-spreading rate of 3 cm/yr, the maximum value on this color scale is 2.25×10^{-7} (kg melt)/(kg mantle)/yr. The panel at right shows the melt fraction F as a function of depth. Melt migration rate is constant and isotropic throughout the domain, such that melts generated at the same distance from the axis will arrive at the axis at the same time (green contours; e.g., for a melt migration rate of 10 m/yr, each successive contour plotted represents points of origin of melts that will arrive at the axis 3000 yrs later). Panels in Figures 2b–2g compare the melting fields for various cases, all on the same spatial and color scales, and showing only the right half of the melting regime. (b) The reference case shown in Figure 2a, with no sea level effect and no lithosphere wedge. (c) The modification of the melting field that results, for a half-spreading rate of 3 cm/yr, when sea level is falling at 2 cm/yr. (d) The corresponding case when sea level is rising at 2 cm/yr. (e) At a half-spreading rate of 3 cm/yr, *Spiegelman and McKenzie* [1987] approximate thickening lithosphere by a wedge with an angle of 24° where flow velocities are horizontal. This panel shows the resulting modification to the melting field for steady sea level: there is no melting above the diagonal line because flow there is horizontal. (f) When sea level is falling at 2 cm/yr, there is melt generation due to decompression in the wedge if the effect of the wedge is only on flow velocities and not on temperature. (g) If the lithospheric wedge is also too cold to melt, then sea level fall will not generate melt in these locations; this panel shows the case of a cold wedge when sea level is falling at 2 cm/yr.

waves, at several times the melt migration velocity [*Spiegelman*, 1993a, 1993b]. Any delay in the driving force due to viscous resistance is therefore negligible compared to damping of the time-dependence of magma flux by melt migration itself.

[13] The mass of melt produced per unit time at each point is the product of the decompression rate and the melt productivity function for the pressure at that point (and the adopted potential temperature). The steady state melt production field (Figure 2) is distributed over a large melting regime (extending to 85 km depth and 120 km horizontally off-axis), but the steady state high melt-production core is compact, centered around 15–30 km depth and within 20 km of the axis horizontally. On the other hand, the sea level-driven decompression

during periods of sea level fall is felt uniformly across the horizontal direction and generates significant off-axis melt, especially where lherzolite residues are present. When a nonzero wedge angle α is adopted, corresponding to the formation of a mechanical boundary layer that changes the plate-driven vertical velocity to zero within the wedge, we need to make a choice about how this affects the melt production. We consider both the case where lithosphere formation is treated as purely a mechanical boundary layer with no effect on sea level-driven melt production and the case where lithosphere formation also involves a thermal boundary layer that brings mantle residue below its local solidus and excludes the possibility of melt generation in this region. All of these cases are illustrated in Figure 2.

2.2. Melt Migration Rate

[14] Magma must migrate from its distributed source locations to the ridge axis before aggregation, fractionation, and eruption. Our model of the melt migration process connects time-dependent driving of melt production to time-dependent delivery of melt to the ridge axis. For simplicity we assume that melts migrate radially (i.e., in three dimensions, along the $-\hat{\mathbf{r}}$ axis of a cylindrical coordinate system) inward toward the ridge axis at a constant rate, v_m; contours of equal origin time for melts arriving at the axis at any given moment are therefore semi-circles (in three dimensions, semi-cylinders) about the axis with linearly increasing radius. This is at best an approximation to the geometry and rates of melt migration, so we consider a wide range of melt migration rate values to assess model sensitivity to this formulation.

[15] We consider melt migration rates between 2 and 50 m/yr. At the slow end, melt migration is constrained by $^{230}Th/^{238}U$ disequilibrium in zero age mid-ocean ridge basalts (MORB), whose $(^{230}Th)/(^{238}U)$ ratios >1 deviate from secular equilibrium [*Richardson and McKenzie*, 1994]. Assuming that the initial partitioning between U and Th happens only in the garnet stability zone (>75 km depth [*Kelemen et al.*, 1997]), melt must migrate to the surface in less than the half-life of ^{230}Th (~75 kyr), giving a minimum melt migration rate of 1 m/yr. Maintenance of $^{230}Th/^{238}U$ disequilibrium through the melting regime by porous flow implies residual melt porosities $\phi < 0.005$ and a melt migration rate faster than the solid upwelling rate by a factor $\sim(F/\phi)$, where F is extent of melting [*Spiegelman and Elliott*, 1993]. For typical F ~0.1 and upwelling rates of 5 cm/yr, this again gives melt velocity of >1 m/yr. On the fast end of the spectrum, the lag between deglaciation and volcanism in Iceland together with the average depth of the melt source implies extraction velocities ≥50 m/yr [*Maclennan et al.*, 2002]. The ^{210}Pb-^{226}Ra disequilibrium observed by *Rubin et al.* [2005] implies that some melts travel even faster, escaping the melting region in decades, but it is unclear whether such rates (~10 km/yr) can be applied uniformly throughout the melting regime. In any case, 50 m/yr melt migration rates are sufficient to demonstrate the fast-migration limit of our model, with prompt and large-amplitude response of magmatic output to millennial-scale sea level variations.

[16] We neglect crustal magmatic or hydrothermal processes that might damp or delay the surface expression of variations in melt delivery to the crust. This is potentially a complicated problem and crustal filtering may well be capable of eliminating any observable expression of such variations on the timescales considered. However, we will examine below a number of data sources that are potentially sensitive to variations in melt flux or heat delivery to the crust on short timescales.

2.3. Model Output

[17] The model is implemented in Mathematica™ (notebook file is available from the authors) as a function that outputs crustal thickness versus time t by integrating melt production (sum of steady state and time-dependent pressure change times productivity) in polar coordinates over the angle from vertical below the ridge to horizontal across-axis and radial distance r from the ridge axis. The melt production term in this integrand is a function of the time-shifted coordinate $(t + r/v_m)$, such that all melts arriving at the axis at t are added together, even though they were produced at increasingly earlier times with increasing r. This formulation limits the length of output crustal thickness time histories to $(t_{max} + (125\ km)/v_m) \leq 140$ kyr, since well-constrained sea level histories are available to only 140 kyr before present. Finally, crustal thickness is estimated from mass of melt per unit time per unit ridge length by dividing by crustal density (assumed constant at 2620 kg/m^3 [*Langmuir et al.*, 1992]) and full-spreading rate. Expressing results this way enables comparison between slow and fast ridges.

3. Model Results and Discussion

[18] We ran a series of sensitivity tests to evaluate (1) the sea level forcing functions from C03 and

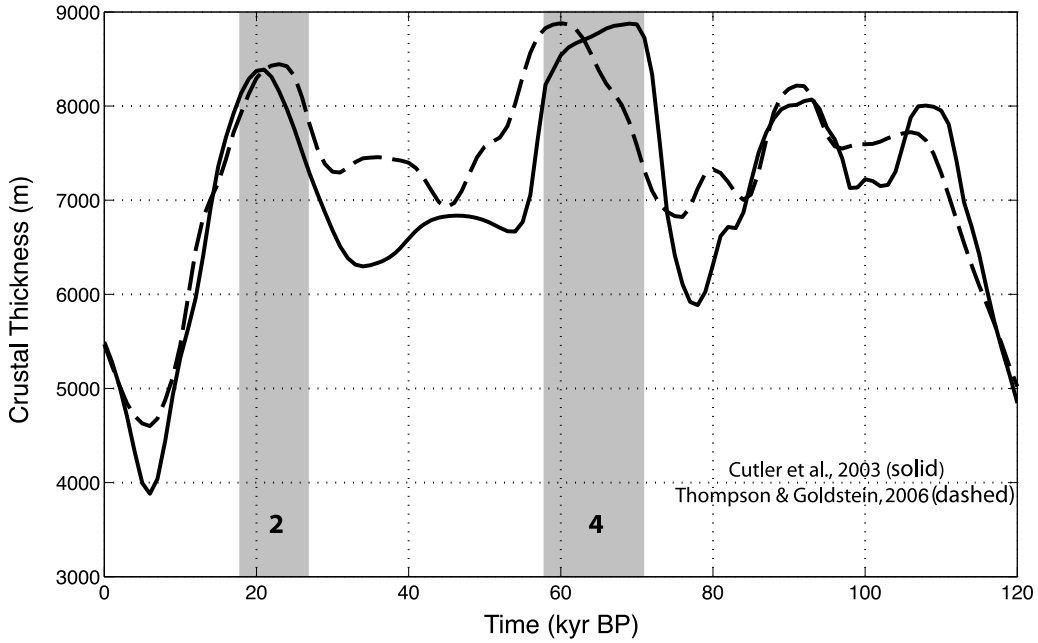

Figure 3. Results of Test A: sea level forcing function. Response of the melting model to changes in sea level for the reference case, where the half-spreading rate is 30 mm/yr and the melt migration rate is 10 m/yr. Results are depicted in terms of crustal thickness, which normalizes magma flux for spreading rate (see text for details). Solid curve is driven by the *Cutler et al.* [2003] sea level history; dashed curve uses the *Thompson and Goldstein* [2006] history. For both cases, magma flux is lowest during the mid-Holocene and highest during MIS 2 and 4. The approximate timing of MIS 2 and 4 are marked with gray vertical bars.

TG06, (2) melt migration rates from 2 m/yr to 50 m/yr; (3) spreading rates from slow (e.g., the northern MAR) to very fast (e.g., the southern EPR); (4) modified corner-flow field accounting for mechanical boundary layer formation using the spreading-rate dependent wedge-angle formulation; (5) modified melt production accounting for thermal boundary layer formation in the wedge-angle lithosphere; and (6) the pHMELTS variable melt productivity function versus constant productivity. Overall, we find that modest changes in hydrostatic pressure driven by ice sheet growth and decay yield substantial alterations in simulated magma flux at mid-ocean ridges relative to steady state conditions. A combination of unfavorable parameters (e.g., very fast spreading, very slow melt migration, and strong damping of off-axis melting by the lithospheric wedge) is necessary to make the sea level effect negligible.

3.1. Reference Case

[19] For the reference case we use the C03 sea level curve, the pHMELTS productivity function, a constant melt migration rate of 10 m/yr, and a half-spreading rate of 30 mm/yr. This is faster than the majority of ridge crests [*Cande et al.*, 1995; *Carbotte and Macdonald*, 1990; *Cogne and Humler*, 2006; *Lonsdale*, 1994] and therefore represents a conservative estimate of the global average response. The reference case has a wedge angle $\alpha = 0$, reflecting the common practice in mid-ocean ridge studies of neglecting lithosphere formation near the axis.

[20] The reference case yields substantial crustal thickness variations over the last glacial cycle (Figure 3). The largest crustal thickness decrease occurs during the last deglaciation, from a maximum (>8 km) just after the LGM to a minimum during the mid-Holocene (<4 km), a peak-to-peak range of 80% of the steady state crustal thickness of 6.3 km. The largest increases occur during MIS 4 and MIS 2, with maxima lagging rapid drops in sea level by about 5000 years due to the 10 m/yr melt migration rate and 50 km average migration distance. As shown below, slower melt migration rates increase the lag between changes in sea level and crustal thickness.

3.2. Test A: Sea Level Forcing Function

[21] Holding melt migration and spreading rate constant, we drove the model using the sea level curve from TG06. In general, the crustal thickness

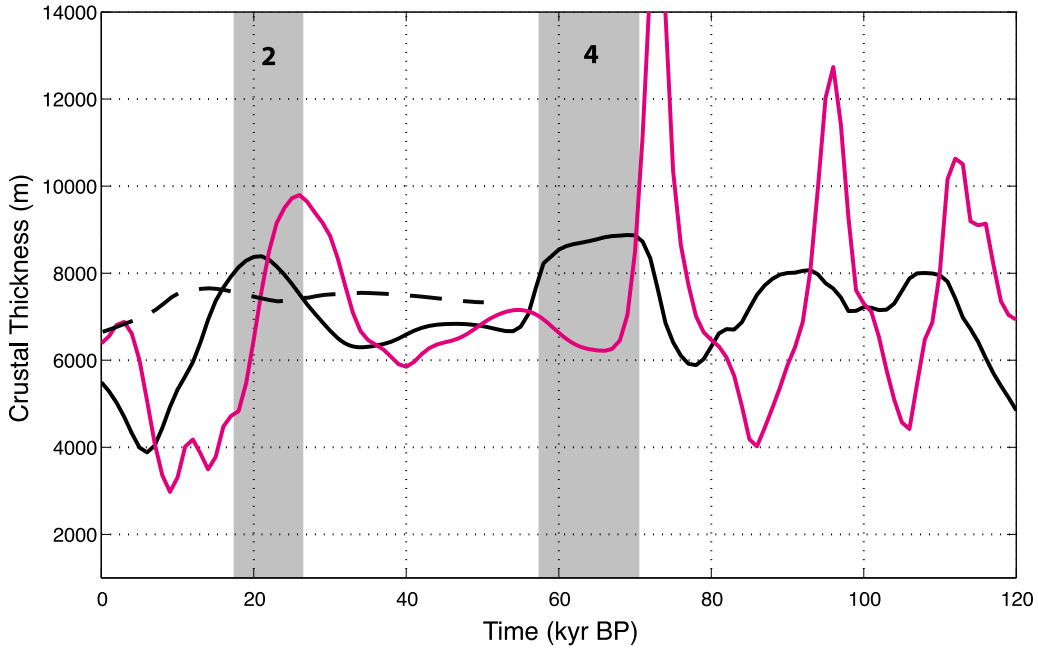

Figure 4. Results of Test B: melt migration rate. Response of the melting model to changes in sea level and variable melt migration rate, including slow (2 m/yr; dashed), intermediate (10 m/yr; black), and fast (50 m/yr; magenta). The *Cutler et al.* [2003] sea level curve and a half-spreading rate of 30 mm/yr were used in each case. The approximate timing of MIS 2 and 4 are marked with gray vertical bars.

results are very similar to the reference case (Figure 3). As before, the largest anomalies are associated with the deglaciation (a ~50% decrease in thickness) and MIS 4 and 2 (~30% increases in thickness). There are some subtle differences. The later drop in sea level near the MIS 5–4 boundary for TG06 results in a ~5 kyr lag in crustal thickness compared to C03. And the MIS 2 anomaly is larger for C03, where lower sea level during MIS 3 creates reduced crustal thickness during this time. Overall, however, the two forcing functions yield broadly consistent changes in crustal thickness.

3.3. Test B: Melt Migration Rate

[22] Next we evaluate sensitivity to melt migration rate. Observational constraints on melt extraction velocities are poor, ranging from >1 m/yr to ≥50 m/yr, so we evaluate three possibilities: 2, 10, and 50 m/yr. We hold spreading rate constant at 30 mm/yr and use the C03 forcing function. For slow melt migration, crustal thickness is about 15% lower during the late Holocene than MIS 2 and 3 (Figure 4). A maximum occurs at approximately 12 kyr BP, lagging the MIS 3/2 transition by ~15 kyr. Slow melt migration velocities thus act to both damp and delay the magmatic signal. If extraction velocities really are this slow, it would imply that evidence for sea level driven magmatism may lag the forcing by ≥10 kyr.

[23] A 50 m/yr melt migration rate yields large and nearly instantaneous crustal thickness response to variations in sea level. The sharp decrease in sea level at the MIS 5/4 boundary creates a peak in magma flux that lags the forcing by <1000 years. The amplitude is large, from a background value of 6 km to a maximum of ~16 km. The magnitude of this anomaly is so large that it seems likely to be readily observable. The scarcity of observations of magma flux variations that we outline in this paper (see below) then suggests that the 50 m/yr migration rate, while perhaps appropriate for Iceland, may not be appropriate for most mid-ocean ridge settings. Also, the 10 m/kyr sea level decrease at the MIS 5/4 boundary may be an overestimate. Only two data points constrain this time interval in C03. The TG06 reconstruction suggests that sea level dropped more slowly, at about 5 m/kyr (Figure 1). More modest rates of sea level decrease yield much smaller crustal thickness anomalies even with rapid melt migration (e.g., MIS 3/2 in Figure 4).

[24] Given melt migration rates between 2 and 50 m/yr, the peak in magmatic activity following the MIS 3/2 transition could occur anywhere

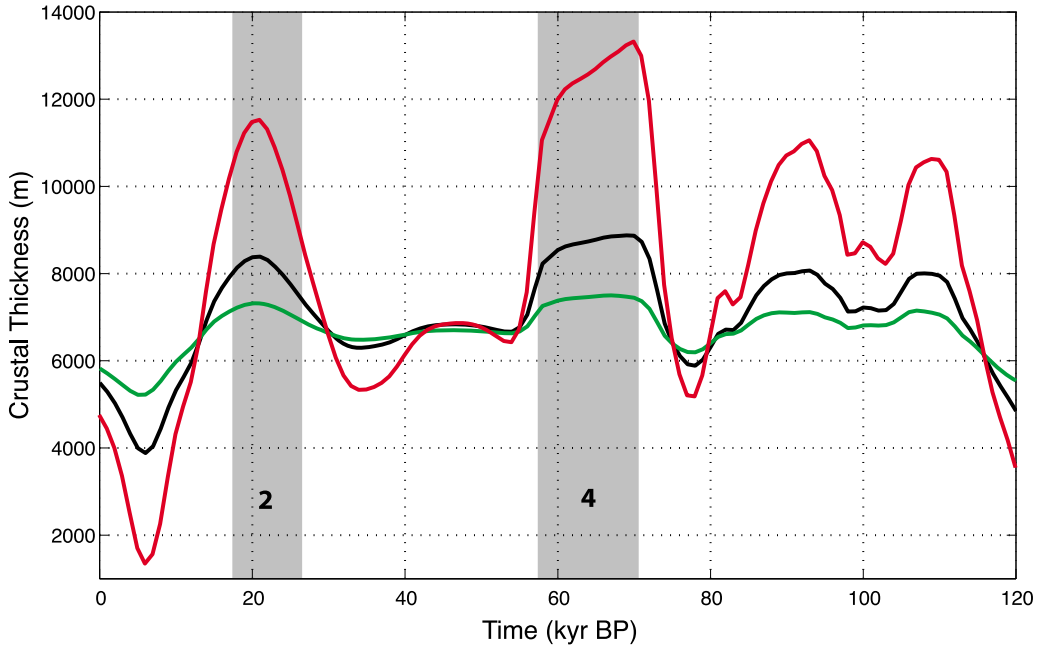

Figure 5. Results of Test C: spreading rate. Response of the melting model to changes in sea level with variable half-spreading rate, including slow (10 mm/yr; red), intermediate (30 mm/yr; black), and fast (75 mm/yr; green). All three cases employ the *Cutler et al.* [2003] sea level curve and a melt-migration rate of 10 m/yr.

between 25 and 10 kyr BP. Positive melt anomalies associated with the LGM could therefore occur during the deglaciation, as sea level was rising. Likewise, the minimum flux to the ridge crest occurred at ~5 kyr BP for our reference case, well after the rapid sea level rise from ~20 to 10 kyr BP (Figure 3). Once melt is generated, segregated and migrating toward the ridge, it is likely to be moving in relatively un-reactive dunite channels [*Kelemen et al.*, 1997], where small increases in pressure will not trigger refreezing. This asymmetry is built into our model: melt only becomes solid at the ridge crest. Hence rising sea levels can reduce the melting rate in parts of the melting regime to zero, but the melting rate is never negative; however, there is no upper limit to the increased melting rate due to falling sea level.

3.4. Test C: Spreading Rate

[25] For this sensitivity test, we hold melt migration rate constant at 10 m/yr and use the C03 sea level curve to simulate melt anomalies for half-spreading rates of 75, 30, and 10 mm/yr. At the MIS 5/4 transition, modeled crustal thickness increases by 1 km for the fast case, 3 km for the intermediate case, and 8 km for the slow case (Figure 5). Similarly, the decrease in crustal thickness associated with the last deglaciation is substantial for all cases, at least a 30% decrease from LGM to mid-Holocene. Our basic scaling exercise indicated that crustal thickness anomalies should be sensitive to spreading rate (Table 1). Here, the across-axis variation in tectonic unloading is depicted more realistically. As a result, sea level loading (or unloading) actually plays a more important role than our scaling estimates predict.

3.5. Test D: Modified Corner Flow With Lithospheric Wedge

[26] *Spiegelman and McKenzie* [1987], in order to use an analytical formulation while including a thickening lithosphere, adopted a linear increase in mechanical boundary layer thickness with distance off-axis as an approximation to the square-root of time curve expected from half-space or (at young age) plate models. They offer a formalism for assigning the wedge angle as a function of spreading rate that best approximates half-space cooling models. Table 1 shows the resulting wedge angles for mantle viscosity of 10^{21} Pa s, solid-melt density difference of 500 kg m^{-3}, and thermal diffusivity 10^{-6} m^2 s^{-1}. We repeated the calculations from test C at three spreading rates with the flow field modified to account for the corresponding wedge

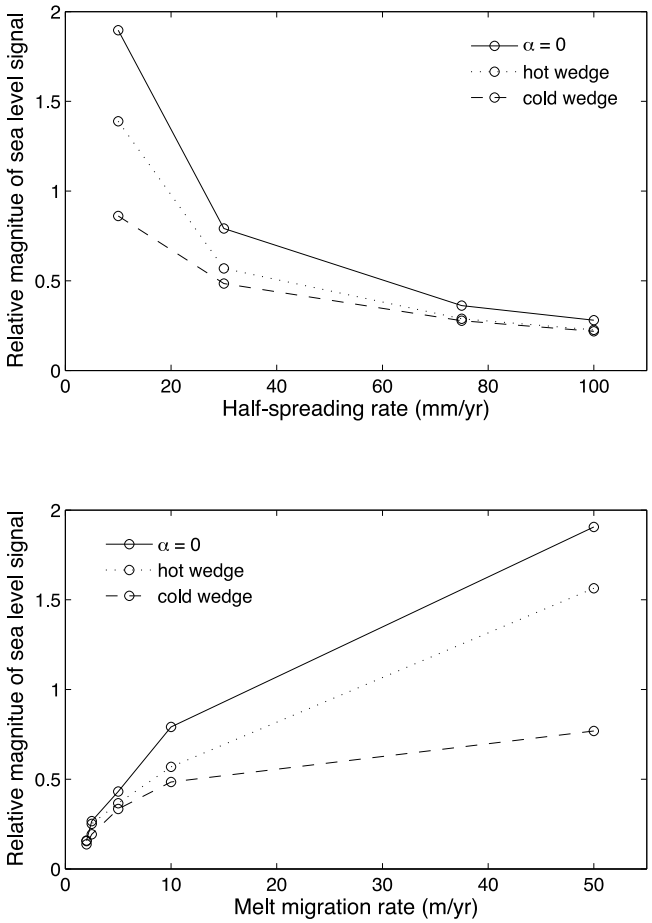

Figure 6. Results of Tests D and E: modified corner flow with warm and cold lithospheric wedges. (top) The effect of sea level variability on relative melt flux (maximum melt flux − minimum melt flux) / (steady state melt flux) versus half spreading rate. The warm wedge case (dotted line) reduces the melt flux anomaly by ~25% relative to the $\alpha = 0$ case (solid line) at slow spreading rates. The cold wedge case yields nearly a 50% reduction in the melt flux anomaly (dashed line) at slow spreading rates. (bottom) The effect of sea level variability on relative melt flux versus melt migration rate. At a melt migration rate of 10 m/yr, including the cold wedge reduces the melt flux anomaly by ~30%. The effect is larger for faster melt extraction velocities.

angles. In the wedge region the vertical velocity and hence the plate-spreading associated rate of pressure change is held to zero, but sea level-driven pressure changes are still felt and can cause melting.

[27] The effect of more concentrated flow field due to a lithospheric wedge reduces the amplitude of predicted melt flux variations somewhat, but the shape of the predicted response and the timing of peaks and troughs are quite similar to the reference case. The effect of the wedge at various spreading rates is shown in Figure 6a using the statistic (maximum melt flux − minimum melt flux) / (steady state melt flux). As predicted, concentration of the upwelling flow into a narrower channel between the wedges of lithosphere decreases the relative importance of sea level variations, but at favorable spreading rate and melt migration rates, the sea level effect remains significant.

3.6. Test E: Modified Thermal Structure With Cold Lithospheric Wedge

[28] A further effect of growth of lithosphere with increasing distance from the ridge axis is cooling of the off-axis upper mantle relative to the upper mantle adiabat. This will decrease and eventually eliminate the melt production in the affected region. Hence, in contrast to the case studied above where the horizontal flow velocities in the lithospheric wedge stop plate-driven melting but sea level-driven melting is still allowed, here we repeat the model with all melting in the lithospheric wedge

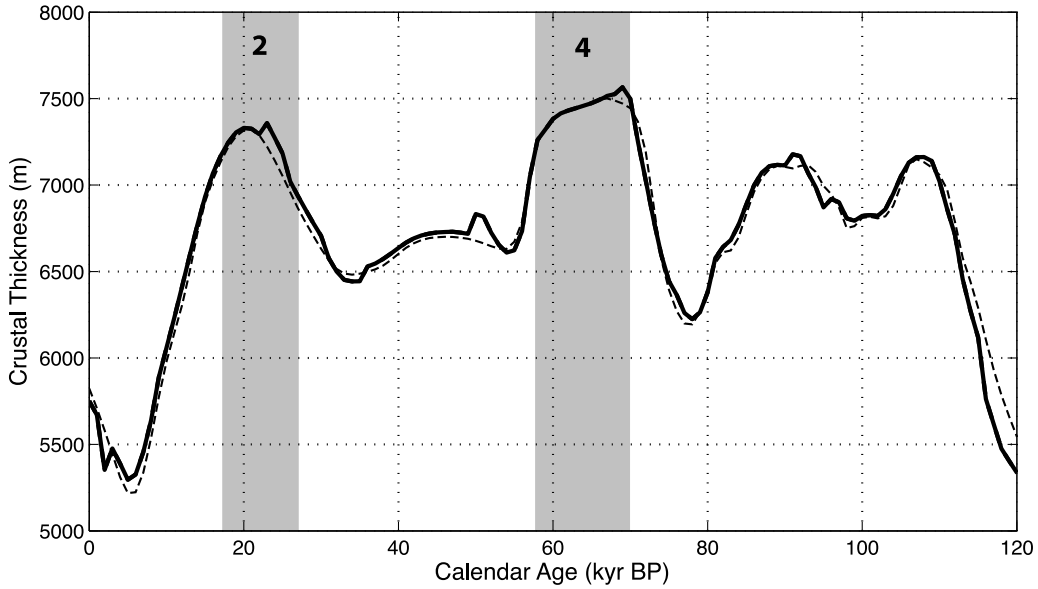

Figure 7. Results of Test F: melt productivity function. Response of the melting model to changes in sea level as a function of melt productivity, including constant productivity with depth (solid) and that based on pHMELTS (dashed). For this test, we ran the case using a fast half-spreading rate (75 mm/yr), an intermediate melt migration rate (10 m/yr), and the *Cutler et al.* [2003] sea level curve. Crustal thickness variations are largely insensitive to the choice of productivity function. The approximate timing of MIS 2 and 4 are marked with gray vertical bars.

turned off. Because a major feature of the reference model is production of substantial amounts of shallow, off-axis melt as sea level falls, this case represents a major perturbation. As Figure 6b shows, the amplitude of melt flux variations is damped in the cold wedge case but it is not eliminated. Another important difference of this model is that the extra melt generated by sea level falls is now generated closer to the axis (in the sub-axial high melt-fraction core of the melting regime) and arrives at the axis sooner. Hence the time lag between sea level variations and magma flux response is decreased.

[29] This sensitivity test shows that the production of shallow, off-axis melt in the reference case (particularly at depths where clinopyroxene remains in the residue) is a substantial part of the sea level effect we describe in the reference case, but it is not the entire story. Notable time-variations in magma flux persist, even when melting in the lithospheric wedge is shut off.

3.7. Test F: Melt Productivity Function

[30] Although the main features of melt production from pHMELTS are theoretically sound, they have not been verified by experiment. Hence it is worthwhile to test the sensitivity of our results to the pHMELTS function. We substituted a constant melt productivity of 0.0148%/MPa and solidus depth of 50 km; at steady state this generates the same crustal thickness as pHMELTS with potential temperature 1344°C. For a 75 mm half-spreading rate, 10 m/yr melt migration, and the C03 sea level forcing, the differences due to productivity functions are minor (Figure 7). Constant productivity is less effective than variable productivity at filtering high-frequency features of the driving function and predicts a few millennial-scale wiggles with amplitudes of ~100 m in crustal thickness, but all major features of the crustal thickness history are identical. We therefore conclude that the sea level forcing effect is largely insensitive to the details of the melt production model.

4. Lines of Evidence to Pursue

[31] Our simulations suggest there should be substantial changes in magma flux to mid-ocean ridges on Milankovitch timescales, particularly if melt-migration rates exceed 2 m/year. Below we discuss proxies that may be sensitive to glacial-interglacial changes in magma flux, including seafloor topog-

raphy, hydrothermal particle fluxes, oceanic Os isotopic ratios, and the radiocarbon content of seawater.

4.1. Seafloor Topography

[32] Although our results suggest crustal thickness should vary by up to 100% at slow-spreading rate ridges (Figure 4), our model does not account for the width of the zone where volcanic and hydrothermal activity is concentrated (i.e., the neo-volcanic zone) or where crustal accretion is generally concentrated (the width of the axial magma chamber). At half-spreading rate of 10 mm/yr, the distance between zones of high (LGM) and low (mid-Holocene) crustal thickness would be ~150 m. However, the neo-volcanic zone for slow-spreading ridges is typically several kilometers wide [*Perfit and Chadwick*, 1998]. Because the distance that the crust would migrate between high and low flux regimes is small relative to the neo-volcanic zone, it is highly unlikely that glacial-interglacial variability in magma flux can be observed using seafloor topography at slow spreading ridges.

[33] At faster ridges, spreading rate may keep pace with changes in sea level-driven magma flux. The lithospheric plates on either side of the southern EPR (~75 mm/yr half-spreading rate) move approximately 1 km in 15,000 years. Typical neo-volcanic zones at fast ridges are 100–200 m wide [*Perfit and Chadwick*, 1998], so intervals of varying eruptive activity may be separated in distance perpendicular to the ridge crest. On the other hand, the half-width of the axial magma chamber reflector observed under the EPR axis is about 1–3 km [*Detrick et al.*, 1987; *Kent et al.*, 1990] and lower crustal accretion is distributed over a similar width [based, e.g., on magnetic transition intervals, *Macdonald*, 1982], so time-variations in overall crustal thickness will be more damped than those in eruptive flux. Furthermore, at fast spreading rates the sea level-driven signal is small relative to lithospheric unloading. For 10 m/yr melt-migration rate and 75 mm/yr half-spreading rate, we simulate that crustal thickness should vary by ~15% on glacial-interglacial timescales (Figure 4). Hence the ridges that may spread quickly enough to record Milankovitch-scale changes in melt flux have the smallest expected anomalies, while those with the largest expected signal do not spread quickly enough.

[34] The ridge-parallel troughs that form abyssal hills may in part represent evidence of periodic magmatism at mid-ocean ridges. In the Pacific, abyssal hills are typically 2–5 km wide, 50–300 m high, and are bounded by faults on each side [*Macdonald et al.*, 1996]. The characteristic spacing of faults on the EPR is approximately 1 km [*Carbotte and Macdonald*, 1994], roughly consistent with that expected from sea level-driven changes in magmatism. As a result, it is tempting to believe the faults represent tectonic evidence supporting the sea level-magmatism link. However, the spacing of abyssal hill faults along the northern EPR is best described by a Poisson distribution, indicative of aperiodic forcing [*Edwards et al.*, 1991]. Fault spacing along the southern EPR and Ecuador Rift are also stochastic in nature, where fault populations are believed to reflect brittle layer thickness [*Carbotte and Macdonald*, 1994]. Although Milankovitch-scale changes in melt flux may be preserved in abyssal hills, isolating this influence from large-scale extensional stresses, thermal contraction of the lithosphere, and local stresses associated with dike intrusion and ridge segmentation will be difficult. The age history of abyssal hills is also poorly constrained by low-resolution magnetic anomalies.

4.2. Hydrothermal Particle Fluxes

[35] Near-surface magma drives hydrothermal convection in young oceanic crust. Estimates of magmatic budget and hydrothermal plume incidence along mid-ocean ridges suggest that hydrothermal activity scales linearly with magma flux [*Baker and German*, 2004]. We hypothesize that intervals of enhanced melt delivery to ridge crests following sea level low stands drove enhanced hydrothermal convection, plume incidence, and flux of hydrothermal fluids. We attempt a global prediction of the magnitude of this effect by combining (1) the mean half-spreading rate along mid-ocean ridges (24 mm/yr) [*DeMets et al.*, 1994], (2) the time series of magma flux as a function of spreading rate from our model, and (3) the *Baker and German* [2004] fit for the relationship between percentage of ridge axis length overlain by a plume (p_h) and magma flux (V_m, in km^3/Ma/km): $p_h = 0.043 + 0.00055V_m$. The steady state global average p_h in this model is 23% (Figure 8). For the case driven by the C03 sea level curve and assuming a 10 m/yr melt migration rate, p_h ranges from a minimum of 15% at in the mid-Holocene to a maximum of 30% shortly after the MIS 5/4 boundary. Below we evaluate whether proxies of hydrothermal activity are consistent with this prediction.

4.2.1. Hydrothermal Metals

[36] Hydrothermal fluids leach metals from the oceanic crust, rise buoyantly, and precipitate sulfides and

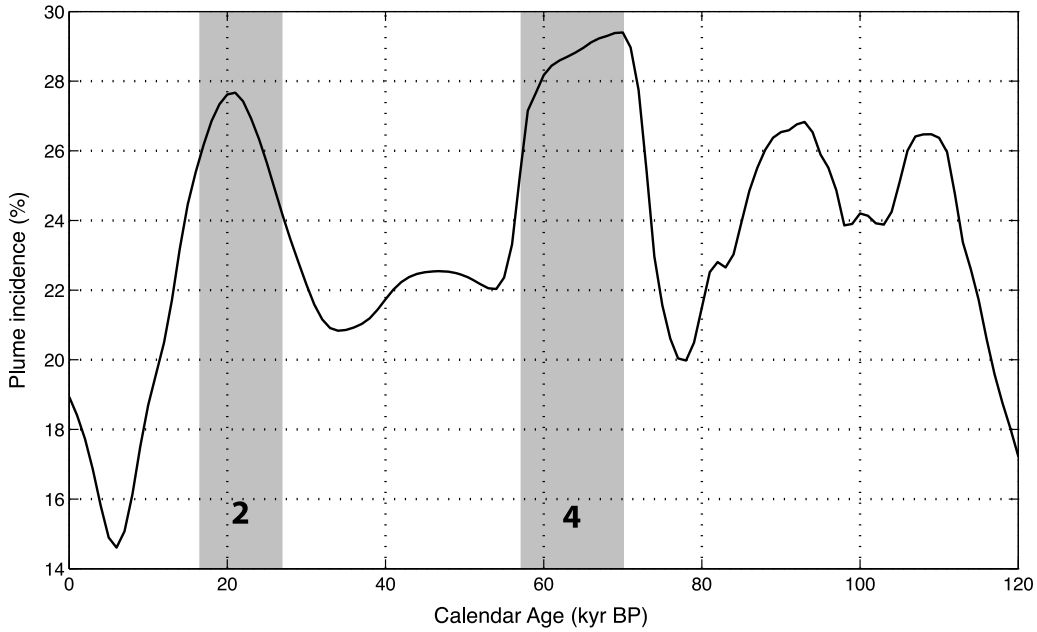

Figure 8. Global prediction of plume incidence based on magma flux from the reference case (Figure 3) and the *Baker and German* [2004] relationship for magma flux (V_m, in km^3/Ma/km) versus percentage of ridge axis length overlain by a plume (p_h) ($p_h = 0.043 + 0.00055V_m$). The steady state global average plume incidence in this model is 23% and the sea level-driven variations range from a minimum of 15% in the mid-Holocene to a maximum of 30% shortly after the MIS 5/4 boundary.

iron-manganese oxyhydroxides upon encountering cold, well-oxygenated seawater. Although the manner of iron precipitation is a matter of ongoing debate [*Toner et al.*, 2009], hydrothermal sediments are clearly enriched in iron and manganese [*Böstrom et al.*, 1969; *Cronan*, 1976; *Heath and Dymond*, 1977]. We hypothesize that intervals of enhanced melt delivery to ridges following sea level low stands drove enhanced hydrothermal convection and greater delivery of iron and manganese to seafloor sediments.

[37] Most studies of hydrothermal sedimentation have focused on the spatial distribution of hydrothermal sediments [*Böstrom et al.*, 1969; *Cronan*, 1976; *Heath and Dymond*, 1977; *Dymond*, 1981] or the behavior of hydrothermal particles within plumes [*German et al.*, 1990, 1991a, 1991b, 2002]. Sedimentary time series of hydrothermal elements exist, but they are typically short or lack adequate age control [*German et al.*, 1993, 1997, 1999]. Longer, well-dated cores used in paleoceanography are not typically taken near vents. Testing our hypothesis requires sediment cores with three key characteristics: (1) proximity to vent sites, (2) adequate accumulation rates to resolve glacial-interglacial variability, and (3) age control based on either radiocarbon or oxygen isotope stratigraphy. Below we discuss cores in the published literature that have been analyzed for hydrothermal metals and meet the above criteria.

4.2.1.1. Galapagos Microplate Hydrothermal Data

[38] In this section, we focus on two cores in the vicinity of the Galapagos microplate, both of which are within 20 km of active spreading centers. The cores were analyzed by *Frank et al.* [1994] for oxygen isotopes, bulk Fe, Mn, Al, and ^{230}Th. Fe/Al and Mn/Al ratios for core KLH068 (1.2°N, 101.6°W, 2870 m water depth) are shown in Figure 9. The oxygen isotope stratigraphy for this core clearly shows Marine Isotope Stages 1–4. Typical pelagic ratios for Fe/Al and Mn/Al are 0.6 and 0.06, respectively [*Chester*, 2000]. Mn/Al for KLH068 rises above background levels during MIS 4 and at the MIS 2–1 boundary. Fe/Al is higher than background pelagic values throughout the record, including maxima during MIS 4, the MIS 3–2 boundary, and the MIS 2–1 boundary. These maxima are broadly consistent with expectations for sea level-driven magmatism.

[39] Thorium-230 flux is also sensitive to hydrothermal sedimentation. Generally, ^{230}Th measures particle flux to the seafloor because it is produced at a nearly constant rate in the water column [*Francois et al.*, 2004; *Yu et al.*, 2001]. However, elevated

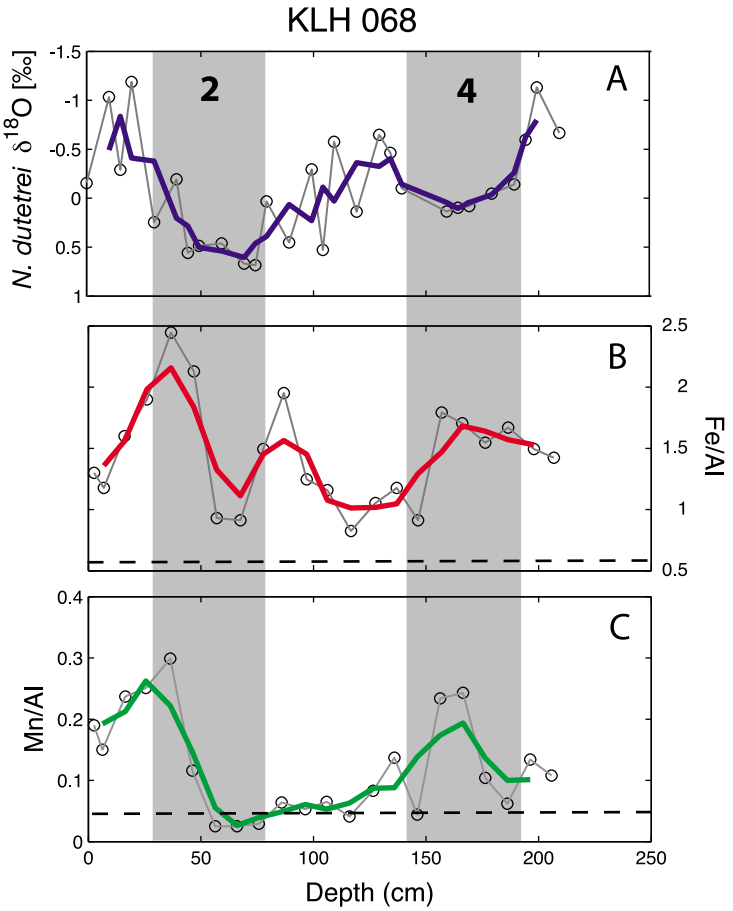

Figure 9. Galapagos microplate sediment data, core KLH068. All data are from *Frank et al.* [1994]. (a) Oxygen isotope stratigraphy based on planktonic foraminifera (*N. dutetrei*), (b) bulk sedimentary Fe/Al, and (c) bulk Mn/Al. Colored lines are 3-point running mean values. Vertical gray bars mark the approximate time of Marine Isotope Stages 2 and 4. Background Mn/Al and Fe/Al ratios for pelagic sediments are 0.06 and 0.6, respectively (dashed lines) [*Chester*, 2000]. Both Mn/Al and Fe/Al are elevated with respect to typical pelagic values during MIS 4 and the MIS 2–1 boundary.

scavenging of ^{230}Th occurs in hydrothermal plumes. Proximal to vent sites, ^{230}Th fluxes can exceed water column production by an order of magnitude, indicating that hydrothermal plumes can act as 'boundary scavenging' locations in the open ocean [*German et al.*, 2002]. Water column flux of ^{230}Th for the water depth of KLH068 should be ~7.5 dpm/cm^2/kyr [*Kadko*, 1980]. Most of downcore data plot at or below this value, with the exception of MIS 2 and the MIS 2–1 boundary, where ^{230}Th flux exceeds 10 dpm/cm^2/kyr (Figure 10b). The combination of high ^{230}Th, Fe, and Mn fluxes suggests that hydrothermal sedimentation was elevated at this time. There are only modest peaks in Fe and Mn flux during MIS 4 despite high Mn/Al and Fe/Al ratios (Figure 9). This suggests that either hydrothermal input was relatively weak or age model error may decrease the sedimentation rate and flux values during MIS 4.

[40] In nearby core KLH093 (1.5°N, 102.1°W, 3259 m water depth), hydrothermal tracers also vary down core, but the oxygen isotope stratigraphy lacks an obvious MIS 4 (Figure 11). Focusing on the younger and more reliable portion of the stratigraphy, there are clear maxima in both Mn/Al and Fe/Al during MIS 2 and the MIS 2–1 boundary. There are also contemporaneous peaks in ^{230}Th and Fe flux (Figure 12). The ^{230}Th flux is approximately twice the estimated water column production rate (8.5 dpm/cm^2/kyr), suggesting the influence of either sediment focusing or hydrothermal scavenging. The correspondence between ^{230}Th flux, Fe flux and high Fe/Al ratios during MIS 2–1 suggest hydrothermal scavenging is the more likely cause. Mn fluxes are different than either those for ^{230}Th or Fe, with a strong peak focused on the deglaciation.

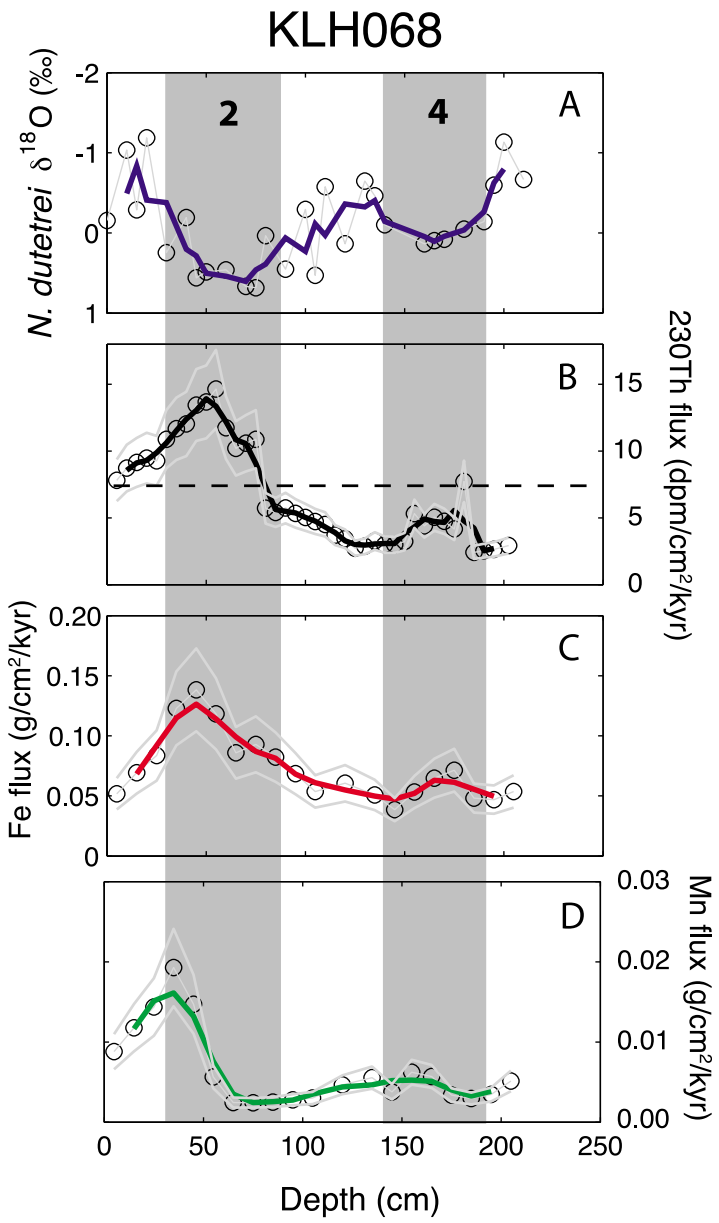

Figure 10. Flux data for core KLH068. (a) Oxygen isotope stratigraphy, (b) ^{230}Th flux (dpm/cm^2/kyr), (c) Fe flux (g/cm^2/kyr), and (d) Mn flux (g/cm^2/kyr). Colored lines are 3-point running mean values. The expected ^{230}Th flux for this water depth is approximately 7.5 dpm/cm^2/kyr (dashed horizontal line). All flux calculations are based on ages inferred from the oxygen isotope stratigraphy. We assume a conservative error of ±30% for the age difference between successive points. This uncertainty dwarfs the errors in dry bulk density, weight percent, and dpm/g reported by *Frank et al.* [1994] and is therefore the primary contributor to the one-sigma flux errors (gray lines). Age model error of a factor or two or larger would be necessary to eliminate the flux maxima at the MIS 2–1 boundary.

4.2.1.2. Hydrothermal Input Versus Diagenetic Remobilization

[41] Many pelagic sediment cores have subsurface Mn peaks that are attributed to diagenetic remobilization and focusing of Mn [*Berger et al.*, 1983; *Froelich et al.*, 1979]. Typically, Mn peaks are found near the sediment-seawater interface, just below the zone of oxygen-rich pore waters. Consumption of Mn oxides in the suboxic zone releases Mn^{2+} that is oxidized at the base of the well-oxygenated surface layer.

[42] The sedimentary Fe/Mn ration can be used to isolate hydrothermal and diagenetic influences on sedimentary Mn. Ridge-flank hydrothermal

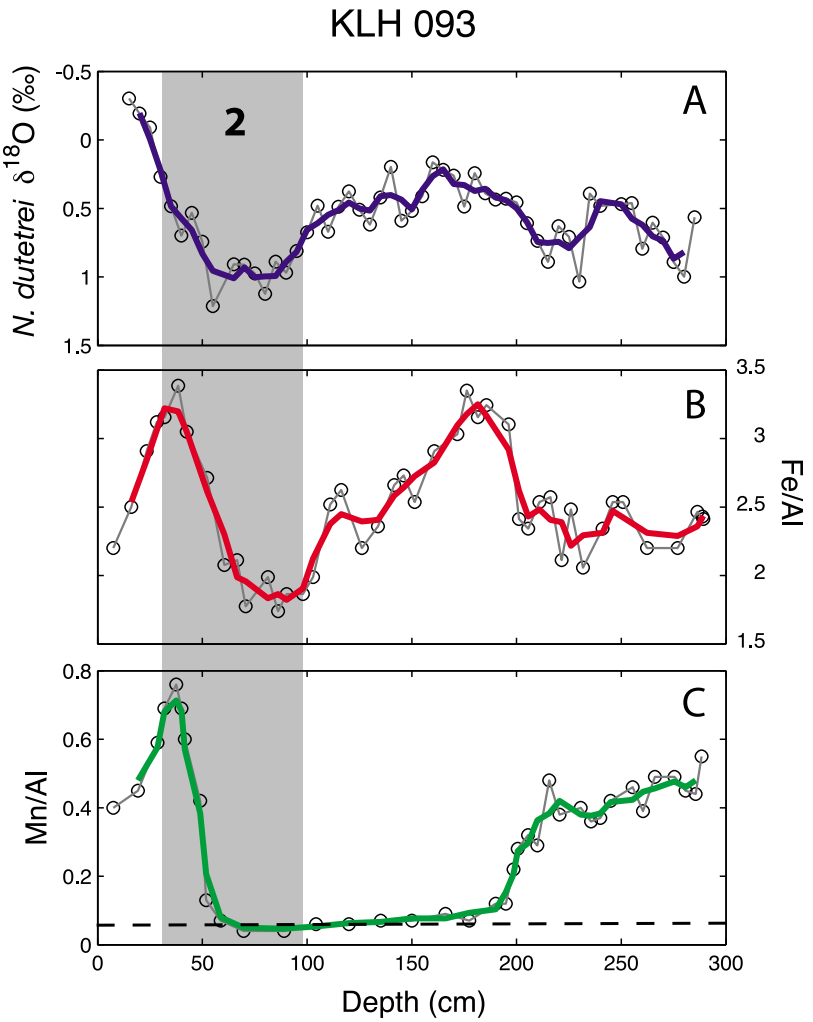

Figure 11. Galapagos microplate sediment data, core KLH093. All data are from *Frank et al.* [1994]. (a) Oxygen isotope stratigraphy based on planktonic foraminifera (*N. dutetrei*), (b) bulk Fe/Al, and (c) bulk Mn/Al. Colored lines are 3-point running mean values. Vertical gray bar marks the approximate interval of Marine Isotope Stage 2. The age of sediments below 150 cm depth is uncertain due to the lack of an obvious MIS 4 and 5. Both Fe/Al and Mn/Al peak during the MIS 2–1 boundary. High Fe/Al ratios between 150 and 200 cm are not matched by elevated Mn/Al ratios, possibly due to diagenetic remobilization of Mn. Background Mn/Al and Fe/Al values for pelagic sediments are 0.06 and 0.6, respectively (dashed lines) [*Chester*, 2000]. Mn/Al for KLH093 is elevated with respect to typical pelagic values from 20 to 50 cm (the MIS 2–1 boundary) and below 200 cm. Low Mn/Al values from 50 to 200 cm are likely due to diagenetic remobilization of Mn (see Figure 13).

sediments from the East Pacific Rise have empirically been shown to have Fe/Mn ratios of 3 ± 1 [*Barrett et al.*, 1987; *Böstrom et al.*, 1969; *Cronan*, 1976; *Dymond*, 1981; *Heath and Dymond*, 1977; *Ruhlin and Owen*, 1986]. Figure 13 displays Fe/Mn data for both Galapagos cores. A linear fit to all Fe/Mn data suggests that down-core Fe/Mn ratios reflect mixing with an end-member with Fe/Mn of 2.1 (r^2 = 0.57). This ratio is consistent with a hydrothermal source, but is on the low end of published values.

[43] The Fe/Mn data in Figure 13 fall into two distinct groups, one with intermediate Fe and low Mn concentrations (open symbols) and another with a broad range of Mn concentrations and a clear linear trend (solid symbols). Nearly all of the low Mn points come from ~50 to 200 cm in core KLH093, where Mn/Al ratios are close to zero (Figure 11). These samples may have been stripped of their Mn by diagenetic remobilization. If we consider the apparently unaffected population of data points (solid symbols in Figure 13), they can be explained by mixing with an end-member with Fe/Mn of ~3.3, which is indistinguishable from hydrothermal Fe/Mn ratios of ~3.5 in several studies [*Barrett et al.*, 1987; *Dymond*, 1981; *Ruhlin and*

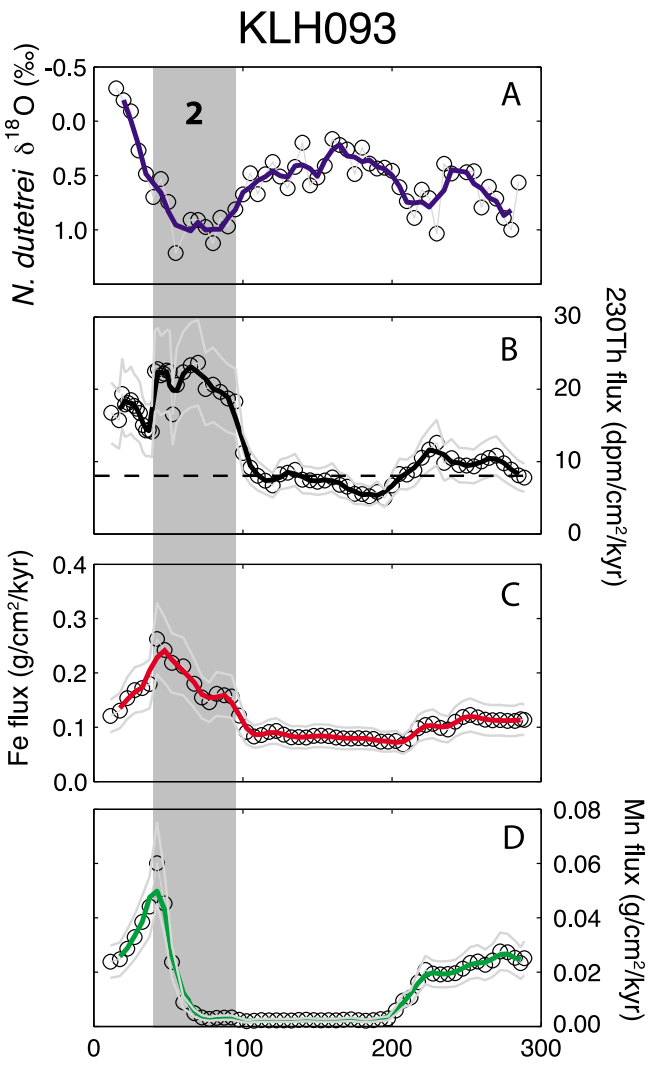

Figure 12. Galapagos microplate flux data for core KLH093. (a) Oxygen isotope stratigraphy, (b) ^{230}Th flux (dpm/cm^2/kyr), (c) Fe flux (g/cm^2/kyr), and (d) Mn flux (g/cm^2/kyr). Colored lines are 3-point running mean values. The expected ^{230}Th flux for this water depth is approximately 8.5 dpm/cm^2/kyr (dashed horizontal line); ^{230}Th fluxes are twice the expected value during the LGM and last deglaciation. Contemporaneous changes in the flux of ^{230}Th and Fe suggest these time series are driven by hydrothermal sedimentation. Low Mn fluxes from 80 to 200 cm may be due to diagenetic remobilization of Mn. Similar to core KLH068, we assume an error of ±30% for the age difference between successive points in KLH093. Because this error is much larger than the errors in dry bulk density, weight percent, and dpm/g reported by *Frank et al.* [1994], age error is the primary driver of the one-sigma flux errors (gray lines). Age model error of a factor or two or larger would be necessary to eliminate the flux maxima at the MIS 2–1 boundary. Low Mn fluxes from 55 to 200 cm are likely due to diagenetic remobilization of Mn (Figure 13).

Owen, 1986]. A linear fit to the data explains 89% of the variance (i.e., $r^2 = 0.89$). These results suggest that the Galapagos microplate Mn/Al and Fe/Al time series primarily reflect initial hydrothermal inputs to the sediment rather than post-depositional diagenetic effects.

4.2.2. Additional Hydrothermal Time Series

[44] Records from the Panama Basin appear to show additional evidence for variable hydrothermal activity during the last glaciation, though they are further from active ridges than the Galapagos microplate cores. A sediment core from ~100 km south of the Costa Rica rift (P7; 2.6°N, 84.0°W; 3085 m water depth) displays elevated Mn/Al ratios during MIS 4 and 2, and elevated Mn and ^{230}Th fluxes during MIS 2 [*Yang et al.*, 1995]. A second core from about ~100 km south of the Galapagos Rift (ME0005A-24JC; 0.0°N, 86.5°W; 2941 m water depth) shows highly elevated ^{230}Th fluxes between 20 and 10 kyr BP [*Kienast et al.*, 2007].

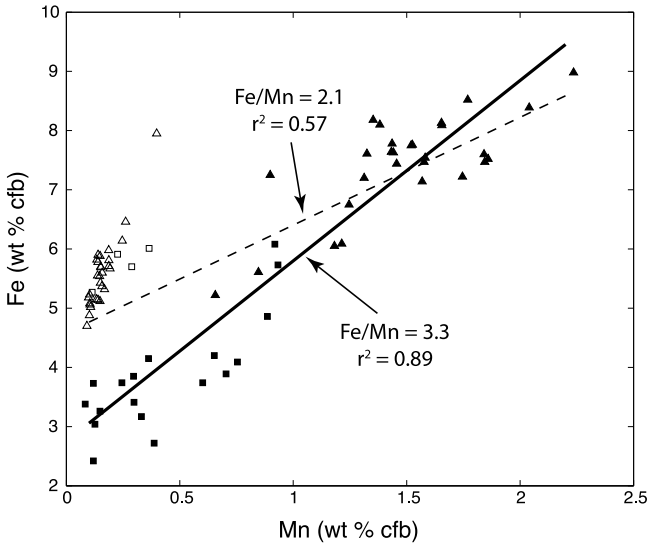

Figure 13. Galapagos microplate sediment data, Mn (wt. % cfb) versus Fe (wt. % cfb) for core KLH068 (squares) and KLH093 (triangles). Weight percentages are calculated on a carbonate-free basis to compensate for the effect of carbonate dilution. Carbonate content for KLH068 ranges from 70 to 80 weight percent, while carbonate content for KLH093 ranges from 75 to 85 weight percent [*Frank et al.*, 1994]. The grouping of low Mn values on the left-hand side of the plot (open squares – KLH068; open triangles – KLH093) suggests these samples have been stripped of their original hydrothermal Mn. The Fe/Mn slope for the remaining samples indicates a end-member Fe/Mn ratio of 3.3, similar to that calculated for hydrothermal ridge-flank sediments in the Pacific [*Dymond*, 1981]. If all data are included in the calculation, the end-member Fe/Mn ratio becomes 2.1 (dashed line).

Although high ^{230}Th fluxes in this core have been interpreted in terms of sediment focusing, their cause is still debated [*Francois et al.*, 2007; *Lyle et al.*, 2007]. We suggest enhanced hydrothermal activity drove elevated ^{230}Th flux to this site during the deglaciation, consistent with elevated Fe/Al and Mn/Al ratios during this interval [*Kienast et al.*, 2007].

[45] At slower spreading rates, melt flux anomalies and presumably the hydrothermal response should be more pronounced. Core SHOM91-KS4 (38.2°N, 30.6°W) near the Lucky Strike segment of the northern MAR [*Auffret et al.*, 1996] displays fluxes of Fe, Mn, Cu, and Zn that were 2–4 times higher during MIS 2 and 4 than during MIS 3 and 5 (Figure 14). Metal fluxes during MIS1 were not evaluated due to apparent diagenetic remobilization in this interval [*Auffret et al.*, 1996]. Thus there appears to be isolated evidence from both the Atlantic and Pacific of enhanced hydrothermal activity associated with even isotope stages.

[46] The largest source of uncertainty associated with the sedimentary hydrothermal tracers is spatial and temporal variability of plumes. Plumes may turn 'on' and 'off' for reasons independent of magma flux to the ridge and plume dispersion will depend on deep ocean currents and Rossby waves [*Speer et al.*, 2003]. The published data summarized here therefore require verification to ensure the anomalies are not simply a function of local plume dynamics. Additional sites from other ridge locations are clearly necessary to demonstrate whether plume events were widespread and broadly synchronous in time.

4.3. Osmium Isotopes

[47] An ideal tracer of hydrothermal activity would be one which (1) is insensitive to spatial and temporal variability of individual plumes, (2) integrates global hydrothermal inputs and, (3) has an oceanic residence time similar to Milankovitch periods. One such candidate is the ^{187}Os/^{188}Os ratio recorded in deep-sea sediments. The osmium isotopic ratio of the modern ocean (~1.05) is believed to reflect a balance of input from radiogenic continental sources (^{187}Os/^{188}Os ~1.2–1.4) and non-radiogenic hydrothermal and extra-terrestrial sources (^{187}Os/^{188}Os ~0.12) [*Peucker-Ehrenbrink and Ravizza*, 2000; *Sharma et al.*, 2000; *Burton et al.*, 2010]. One solution to the modern oceanic ^{187}Os/^{188}Os mass balance involves input from continental (67%), mid-ocean ridge (14%), ridge

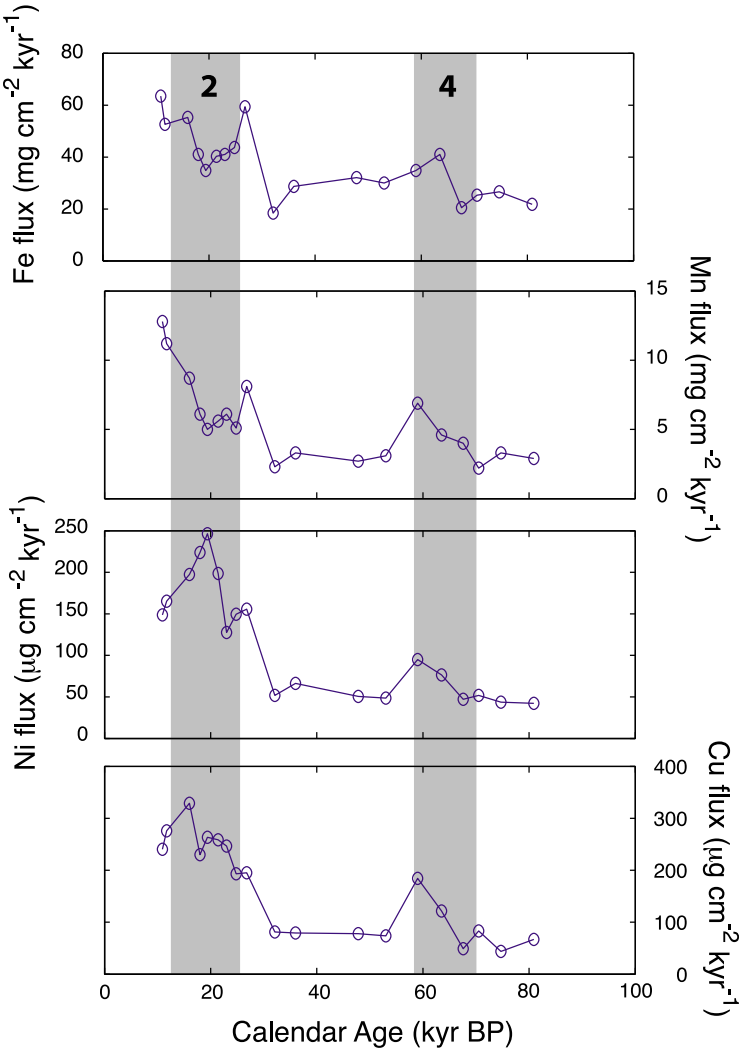

Figure 14. Results for core SHOM91-KS4 from the northern Mid-Atlantic Ridge, near the Lucky Strike segment (38.2°N, 30.6°W). All data are from *Auffret et al.* [1996]. Fluxes of Fe, Mn, Cu, and Zn are elevated during MIS 4, MIS 2, and at the MIS 2–1 boundary. Vertical gray bars mark approximate positions of MIS 2 and 4 as determined by *Auffret et al.* [1996].

flank (13%), and extraterrestrial (6%) osmium sources [*Burton et al.*, 2010].

[48] Sedimentary Os isotopic records from the last glacial cycle generally show that oceanic $^{187}Os/^{188}Os$ was less radiogenic during MIS 6, 4, and the MIS 2–1 boundary (Figure 15). The Os isotope ratio ranges from 0.90 to 1.00 during glacial times and 1.00 to 1.05 during interglacial times. Scatter in the data is likely due to heterogeneous seawater Os isotopic composition and analytical error associated with isolating the hydrogenous component of bulk sediment [*Peucker-Ehrenbrink and Ravizza*, 2000; *Oxburgh*, 2001]. The Os signal has been interpreted to represent decreased continental weathering during glacial maxima and reduced input of radiogenic Os to the oceans [*Dalai et al.*, 2005; *Oxburgh et al.*, 2007; *Williams and Turekian*, 2004]. For example, the glacial $^{187}Os/^{188}Os$ ratio of 0.95 can be achieved by reducing the riverine Os flux by 30% and decreasing its Os isotopic ratio by 4% [*Burton et al.*, 2010].

[49] Explanations of the glacial-interglacial Os signal in terms of continental weathering are based on the assumption that hydrothermal Os flux has remained constant through time. Here instead we speculate that the hydrothermal Os flux increased during glacial maxima, which would have driven the oceanic Os isotopic ratio toward non-radiogenic values. Although the riverine flux of Os must have varied on Milankovitch timescales, uncertainty in the rate of continental weathering, transport of Os to the oceans, and its isotopic composition preclude a detailed accounting of the terrestrial role in the oceanic Os

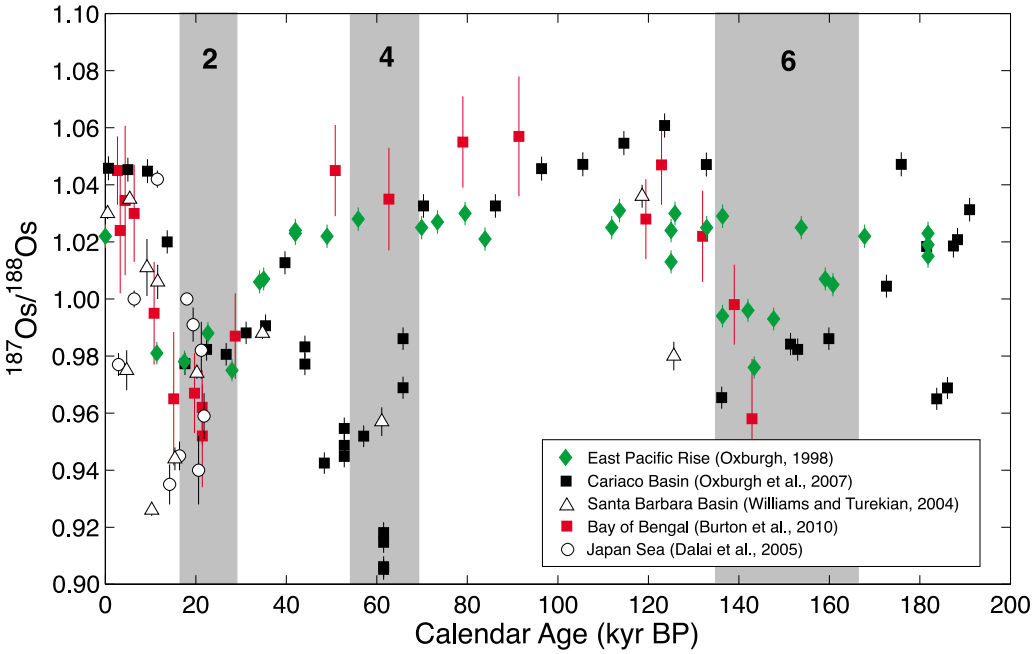

Figure 15. Summary plot of the oceanic osmium isotopic ratio for the last 200,000 years, including data from *Oxburgh* [1998] (green diamonds), *Williams and Turekian* [2004] (white triangles), *Dalai et al.* [2005] (white circles), *Oxburgh et al.* [2007] (black squares), and *Burton et al.* [2010] (red squares). Despite considerable scatter in the available data, $^{187}Os/^{188}Os$ values are generally lower during MIS 6, 4, 2, and the MIS 2–1 transition.

budget. Given the potential connection between sea level and hydrothermal activity, the possibility of variable hydrothermal Os output should also be considered.

[50] Our model results suggest that melt production at intermediate spreading rate ridges was approximately 50% higher than today during the LGM and deglaciation (Figure 3). If Os flux scales linearly with magma flux, this would translate a global increase in hydrothermal Os input of 50%. Based on the oceanic Os budget outlined by *Burton et al.* [2010], this would cause a decrease in the oceanic $^{187}Os/^{188}Os$ ratio of 0.06, about half of the glacial-interglacial signal. If Os-rich peridotites at slow spreading centers account for a disproportionate flux of non-radiogenic Os [*Sharma et al.*, 2007; *Burton et al.*, 2010], the larger melting response at these locations could amplify the hydrothermal influence on the oceanic Os ratio.

[51] It is also useful to evaluate the timing of osmium isotopic variability. If continental weathering acts as the primary control on oceanic $^{187}Os/^{188}Os$ variability, it is reasonable to expect that oceanic $^{187}Os/^{188}Os$ would decrease during sea level low stands, when landmasses are covered in ice and delivery of radiogenic Os to the ocean is presumably reduced [*Oxburgh et al.*, 2007]. Sea level reconstructions indicate that ice volume increased from 75 to 60 kyr BP, remained more or less stable until about 30 kyr BP, and then increased again during the Last Glacial Maximum (Figure 1). The composite Os isotopic record is generally consistent with this pattern (Figure 15), except for the increase in $^{187}Os/^{188}Os$ from 60 to 40 kyr BP recorded in both the Cariaco Basin [*Oxburgh et al.*, 2007] and Santa Barbara Basin [*Williams and Turekian*, 2004]. If ice volume was in fact steady during this time interval, it seems unlikely that weathering would have driven higher $^{187}Os/^{188}Os$ ratios at these locations. Curiously, other sites show very little signal in this interval, suggesting that the ocean was not in steady state with respect to $^{187}Os/^{188}Os$ or that some of the records do not reliably record the osmium isotopic composition of ocean water.

[52] Our model predicts two major peaks in melt production during the past 80 kyr, centered at approximately 60 and 20 kyr BP (Figure 3). If hydrothermal Os input responded to enhanced melt production, then oceanic $^{187}Os/^{188}Os$ should become less radiogenic at these times, similar to the observed pattern. The timing of the modeled melt production related to sea level is therefore a reasonable match to the Os isotopic record. The magnitude of the isotopic anomalies is also consistent with the modeled melt anomalies, assuming that Os flux scales linearly with

magma flux. Thus it is plausible that the oceanic Os records may reflect the sea level-induced changes in magmatism at mid-ocean ridges.

4.4. Radiocarbon Signature of Hydrothermal Fluids

[53] Hydrothermal plumes are rich in dissolved inorganic carbon (DIC) from the degassing of melt beneath ridge crests [*Pineau and Javoy*, 1994]. High-temperature (250–400°C) hydrothermal fluid DIC concentrations range from 3 to 285 mmol/kg (median 20 mmol/kg) [*Butterfield et al.*, 2003; *Proskurowski et al.*, 2004] compared to typical deep-sea DIC values of 2 mmol/kg. At the Juan de Fuca Ridge, the DIC concentration in high-temperature plumes approaches 100 mmol/kg following magmatic events [*Proskurowski et al.*, 2004], a factor of 50 larger than typical deep ocean values. These same fluids have a $\Delta^{14}C$ of −980 ± 10‰ (±1σ) [*Proskurowski et al.*, 2004]. A minor contribution of carbon from either seawater or deep-sea sediment prevents the samples from being completely radiocarbon 'dead' ($\Delta^{14}C = -1000$‰). Enhanced magma flux and degassing at mid-ocean ridges may therefore create oceanic $\Delta^{14}C$ anomalies.

[54] Four separate locations within 400 km of ridge crests display large excursions in seawater $\Delta^{14}C$ during the last 25,000 years. A foraminiferal $\Delta^{14}C$ record from 705 m water depth near the northern EPR displays a −200‰ anomaly from 18 to 12 kyr BP [*Marchitto et al.*, 2007]. Another record from 620 m water depth south of the Galapagos Spreading Center displays a −300‰ anomaly during the LGM and deglaciation [*Stott et al.*, 2009]. Similar anomalies have been noted from 1200 to 2300 m water depth east of the Rejkyanes Ridge [*Thornalley et al.*, 2011] and from 600 to 800 m water depth near the Sheba Ridge in the Arabian Sea [*Bryan et al.*, 2010]. The $\Delta^{14}C$ signals cannot be easily explained by changes in atmospheric ^{14}C production rate [*Broecker and Barker*, 2007] or the influence of ^{14}C-depleted carbon from an isolated abyssal ocean reservoir [*Broecker et al.*, 2008; *De Pol-Holz et al.*, 2010; *Rose et al.*, 2010; *Broecker and Clark*, 2010; *Sortor and Lund*, 2011; *Lund et al.*, 2011]. It appears that an alternative mechanism is necessary to account for the intermediate-depth $\Delta^{14}C$ anomalies during the last deglaciation.

[55] We speculate the enigmatic radiocarbon anomalies may reflect the influence of carbon from the mantle. Because of the high carbon content and low $\Delta^{14}C$ of hydrothermal fluid, relatively small amounts of fluid are required to yield large radiocarbon anomalies. By mass balance, a $\Delta^{14}C$ anomaly of −250‰ would require adding about 3% hydrothermal fluid by mass to ocean water, assuming $[DIC]_{ocean}$ = 2 mmol/kg and $[DIC]_{hydrothermal}$ = 20 mmol/kg. If $[DIC]_{hydrothermal}$ = 100 mmol/kg, then approximately 0.5% hydrothermal fluid is required.

[56] In the modern equatorial Pacific, the largest ^{3}He signal occurs within several hundred kilometers of the EPR and is centered at water depths of 2–3 km [*Lupton*, 1998]. If the depth of hydrothermal plumes during the last deglaciation was similar to today, then hydrothermal activity is an unlikely source of the $\Delta^{14}C$ anomalies at thermocline depths. Plumes related to enhanced mid-ocean ridge magmatism may have reached higher in the water column, however. So-called 'plume events' in the modern ocean produce unusually large temperature anomalies that reside higher in the water column than typical hydrothermal plumes [*Lupton et al.*, 1999]. A magmatic event at Juan de Fuca Ridge produced a plume ~20 km in lateral diameter and 600 m thick, with an upper edge reaching more than 1000 m above the seafloor [*Baker et al.*, 1987]. Another large event in the Arabian Sea formed a plume ~70 km in diameter and 500 m thick that reached approximately 1200 m above the seafloor [*Murton et al.*, 2006]. Plume size, heat content, and rise height therefore vary considerably in the modern ocean. Although plumes reaching water depths as shallow as 600 m seems unlikely, we are unable to automatically rule out this possibility based on modern observations.

5. Conclusions

[57] During the last glacial cycle, growth of continental ice sheets caused eustatic sea level to decrease ~50 m at both the MIS 5/4 and 3/2 boundaries. The resulting rate of mantle depressurization was comparable to that from seafloor spreading, meaning that declining sea level should have enhanced melting beneath the global mid-ocean ridge system. The reverse should have occurred during the last deglaciation when sea level rose by 120 m. The largest changes in mantle decompression melting should occur at slow spreading ridges, where the sea level pressure effect is a larger proportion of the total pressure field.

[58] We model the effect of oceanic hydrostatic pressure on melting beneath mid-ocean ridges

using published records of sea level for the last 140,000 years. As expected, our simulations show that peaks in magma flux follow drops in sea level. The minimum simulated flux occurs during the mid-Holocene, following rapid sea level rise at the MIS 2/1 boundary. Our results are largely insensitive to the choice of sea level forcing function or melt production algorithm. The model output is highly sensitive to melt extraction and seafloor spreading rates, however. Slow extraction rates (≤2 m/yr) yield minimal changes in melt flux, whereas moderate to fast extraction velocities (≥10 m/yr) yield changes in flux of ≥15%. At fast seafloor spreading rates, modeled changes in flux are modest, about 15% relative to the long-term average. At slow half-spreading rates, we find that magma flux varies by nearly 100%. This signal could be strongly damped by rapidly thickening cold lithosphere off-axis or by crustal filtering.

[59] Evidence in support of sea level-driven magmatism is sparse and circumstantial. Direct confirmation may exist in seafloor topography, but the rate of spreading at most ridges is slow relative to glacial-interglacial timescales. At fast ridges, the pressure effect from sea level is small compared to mantle unloading from seafloor spreading, so the changes in magma flux through time should be small. It will also be difficult to extract periodic changes in magma flux from the stochastic background of ridge-parallel faulting that characterizes seafloor topography. Poor age control for topographic features presents another serious hurdle for linking records of sea level to hard evidence for changes in magma flux.

[60] In the modern ocean, hydrothermal activity at mid-ocean ridges appears to scale with magma flux. It may therefore be possible to estimate changes in magmatic activity through time using hydrothermal tracers preserved in ocean sediments. Unlike seafloor topography, marine sediments can be accurately dated using radiocarbon and oxygen isotope stratigraphy. Of the published hydrothermal records we review, records near the Galapagos microplate and the Lucky Strike segment of the Mid-Atlantic Ridge are the best constrained. In both cases, Fe and Mn fluxes were elevated during MIS 4 and the MIS 2–1 boundary, consistent with the timing of increased melt flux in our model runs. Although the records may be complicated by diagenetic remobilization, the downcore Fe/Mn ratio suggests the signal is primarily hydrothermal in origin. A conclusive link between sea level and hydrothermal variability will require a far larger network of sediment cores from ridge axes around the globe.

[61] Unlike isolated records of Fe and Mn flux from ridge crest sediments, time series of the oceanic osmium isotopic composition may serve as a global integrator of hydrothermal activity. Oceanic $^{188}Os/^{187}Os$ was generally lower during MIS 4, MIS 2, and the MIS 2–1 transition. Although this pattern has been interpreted to represent lower continental weathering during intervals of ice sheet growth, enhanced hydrothermal activity may also play a role. Progress on this front will require improved understanding of the modern Os budget and an independent assessment of continental weathering during the last glacial cycle.

[62] Finally, we suggest that oceanic radiocarbon anomalies of the last deglaciation may be driven by input of carbon from the mantle. Large negative $\Delta^{14}C$ anomalies near mid-ocean ridges could be due to the input of small amounts of radiocarbon 'dead' hydrothermal fluid. The depth of the deglacial radiocarbon anomalies appears to be inconsistent with the depth of neutrally buoyant hydrothermal plumes in the modern ocean, with the exception of rare plume events. Further evaluation of this possibility will require a far larger array of $\Delta^{14}C$ reconstructions from sites at a range of water depths and distances from mid-ocean ridges.

[63] Individually, none of the proxies we discuss provide convincing evidence in support of the sea level-magmatism link. Collectively, however, they are suggestive. A more conclusive test of the hypothesis will require a community-wide effort, spanning the disciplines of mantle petrology, tectonics, hydrothermal geochemistry, and paleoceanography. If magma flux is linked to sea level, it would suggest that (1) climate variability directly impacts melting of the upper mantle, (2) the rate of element cycling through the modern mid-ocean ridge system is probably not representative of Pleistocene averages, and (3) magma CO_2 flux to mid-ocean ridges increases at the time of glacial terminations, potentially acting as a negative feedback on ice sheet size.

Acknowledgments

[64] We thank John Maclennan, Donna Blackman, and three anonymous reviewers for their constructive criticism. We would also like to thank Peter Huybers, Marc Spiegelman, and John Southon for comments and suggestions. Funding for this project was in part provided by the University of Michigan (D. Lund).

References

Asimow, P. D., M. M. Hirschmann, and E. M. Stolper (1997), An analysis of variations in isentropic melt productivity, *Philos. Trans. R. Soc. London, Ser. A*, *355*, 255–281, doi:10.1098/rsta.1997.0009.

Asimow, P. D., M. M. Hirschmann, and E. M. Stolper (2001), Calculation of peridotite partial melting from thermodynamic models of minerals and melts. IV. Adiabatic decompression and the composition and mean properties of mid-ocean ridge basalts, *J. Petrol.*, *42*(5), 963–998, doi:10.1093/petrology/42.5.963.

Asimow, P. D., J. E. Dixon, and C. H. Langmuir (2004), A hydrous melting and fractionation model for mid-ocean ridge basalts: Application to the Mid-Atlantic Ridge near the Azores, *Geochem. Geophys. Geosyst.*, *5*, Q01E16, doi:10.1029/2003GC000568.

Auffret, G. A., et al. (1996), Record of hydrothermal activity in sediments from the Mid-Atlantic Ridge south of the Azores, *C. R. Acad. Sci.*, *323*(7), 583–590.

Baker, E. T., and G. R. German (2004), On the global distribution of hydrothermal vent fluids, in *Mid-Ocean Ridges: Hydrothermal Interactions Between the Lithosphere and Oceans*, *Geophys. Monogr. Ser.*, vol. 148, edited by C. R. German, J. Lin, and L. M. Parson, pp. 245–266, AGU, Washington, D. C., doi:10.1029/148GM10.

Baker, E. T., G. J. Massoth, and R. A. Feely (1987), Cataclysmic hydrothermal venting on the Juan-De-Fuca ridge, *Nature*, *329*(6135), 149–151, doi:10.1038/329149a0.

Bard, E., B. Hamelin, and R. G. Fairbanks (1990a), U-Th ages obtained by mass-spectrometry in corals from Barbados: Sea level during the past 130,000 years, *Nature*, *346*(6283), 456–458, doi:10.1038/346456a0.

Bard, E., B. Hamelin, R. G. Fairbanks, and A. Zindler (1990b), Calibration of the ^{14}C timescale over the past 30,000 years using mass-spectrometric U-Th ages from Barbados corals, *Nature*, *345*(6274), 405–410, doi:10.1038/345405a0.

Barrett, T. J., P. N. Taylor, and J. Lugowski (1987), Metalliferous sediments from DSDP Leg 92: The East Pacific Rise transect, *Geochim. Cosmochim. Acta*, *51*(9), 2241–2253, doi:10.1016/0016-7037(87)90278-X.

Batchelor, G. K. (1967), *An Introduction to Fluid Dynamics*, Cambridge Univ. Press, Cambridge, U. K.

Berger, W. H., R. C. Finkel, J. S. Killingley, and V. Marchig (1983), Glacial-Holocene transition in deep-sea sediments: Manganese-spike in the east-equatorial pacific, *Nature*, *303*(5914), 231–233, doi:10.1038/303231a0.

Bintanja, R., R. S. W. van de Wal, and J. Oerlemans (2005), Modelled atmospheric temperatures and global sea levels over the past million years, *Nature*, *437*(7055), 125–128, doi:10.1038/nature03975.

Böstrom, K., M. N. Peterson, O. Joensuu, and D. E. Fisher (1969), Aluminum-poor ferromanganoan sediments on active oceanic ridges, *J. Geophys. Res.*, *74*(12), 3261–3270, doi:10.1029/JB074i012p03261.

Braun, M. G., G. Hirth, and E. M. Parmentier (2000), The effects of deep damp melting on mantle flow and melt generation beneath mid-ocean ridges, *Earth Planet. Sci. Lett.*, *176*(3–4), 339–356, doi:10.1016/S0012-821X(00)00015-7.

Broecker, W., and S. Barker (2007), A 190‰ drop in atmosphere's Δ^{14}C during the "Mystery Interval" (17.5 to 14.5 kyr), *Earth Planet. Sci. Lett.*, *256*(1–2), 90–99, doi:10.1016/j.epsl.2007.01.015.

Broecker, W. S., and E. Clark (2010), Search for a glacial-age ^{14}C-depleted ocean reservoir, *Geophys. Res. Lett.*, *37*, L13606, doi:10.1029/2010GL043969.

Broecker, W., E. Clark, and S. Barker (2008), Near constancy of the Pacific Ocean surface to mid-depth radiocarbon-age difference over the last 20 kyr, *Earth Planet. Sci. Lett.*, *274*(3–4), 322–326, doi:10.1016/j.epsl.2008.07.035.

Bryan, S. P., T. M. Marchitto, and S. J. Lehman (2010), The release of C-14-depleted carbon from the deep ocean during the last deglaciation: Evidence from the Arabian Sea, *Earth Planet. Sci. Lett.*, *298*(1–2), 244–254, doi:10.1016/j.epsl.2010.08.025.

Burton, K. W., A. Gannoun, and I. J. Parkinson (2010), Climate driven glacial-interglacial variations in the osmium isotope composition of seawater recorded by planktic foraminifera, *Sci. Lett. Earth Planet*, *295*, 58–68, doi:10.1016/j.epsl.2010.03.026.

Butterfield, D. A., W. E. Seyfried, and M. D. Lilley (2003), Composition and evolution of hydrothermal fluids, in *Energy and Mass Transfer in Marine Hydrothermal Systems*, edited by P. E. Halbach, V. Tunnicliffe, and J. R. Hein, pp. 123–162, Dahlem Univ. Press, Berlin.

Cande, S. C., C. A. Raymond, J. Stock, and W. F. Haxby (1995), Geophysics of the Pitman fracture zone and Pacific-Antarctic plate motions during the Cenozoic, *Science*, *270*(5238), 947–953, doi:10.1126/science.270.5238.947.

Carbotte, S. M., and K. C. Macdonald (1990), Causes of variation in fault-facing direction on the ocean-floor, *Geology*, *18*(8), 749–752, doi:10.1130/0091-7613(1990)018<0749:COVIFF>2.3.CO;2.

Carbotte, S. M., and K. C. Macdonald (1994), Comparison of seafloor tectonic fabric at intermediate, fast, and super fast spreading ridges: Influence of spreading rate, plate motions, and ridge segmentation on fault patterns, *J. Geophys. Res.*, *99*(B7), 13,609–13,631, doi:10.1029/93JB02971.

Chester, R. (2000), *Marine Geochemistry*, 506 pp., Blackwell Sci, Oxford, U. K.

Clark, P. U., A. S. Dyke, J. D. Shakun, A. E. Carlson, J. Clark, B. Wohlfarth, J. X. Mitrovica, S. W. Hostetler, and A. M. McCabe (2009), The Last Glacial Maximum, *Science*, *325*(5941), 710–714, doi:10.1126/science.1172873.

Cogne, J. P., and E. Humler (2006), Trends and rhythms in global seafloor generation rate, *Geochem. Geophys. Geosyst.*, *7*, Q03011, doi:10.1029/2005GC001148.

Cronan, D. S. (1976), Basal metalliferous sediments from the eastern Pacific, *Geol. Soc. Am. Bull.*, *87*(6), 928–934, doi:10.1130/0016-7606(1976)87<928:BMSFTE>2.0.CO;2.

Cutler, K. B., R. L. Edwards, F. W. Taylor, H. Cheng, J. Adkins, C. D. Gallup, P. M. Cutler, G. S. Burr, and A. L. Bloom (2003), Rapid sea-level fall and deep-ocean temperature change since the last interglacial period, *Earth Planet. Sci. Lett.*, *206*(3–4), 253–271, doi:10.1016/S0012-821X(02)01107-X.

Dalai, T. K., K. Suzuki, M. Minagawa, and Y. Nozaki (2005), Variations in seawater osmium isotope composition since the last glacial maximum: A case study from the Japan Sea, *Chem. Geol.*, *220*(3–4), 303–314, doi:10.1016/j.chemgeo.2005.04.012.

DeMets, C., R. G. Gordon, D. F. Argus, and S. Stein (1994), Effect of recent revisions to the geomagnetic reversal time scale on estimates of current plate motions, *Geophys. Res. Lett.*, *21*(20), 2191–2194, doi:10.1029/94GL02118.

De Pol-Holz, R., L. Keigwin, J. Southon, D. Hebbeln, and M. Mohtadi (2010), No signature of abyssal carbon in

intermediate waters off Chile during deglaciation, *Nat. Geosci.*, *3*(3), 192–195, doi:10.1038/ngeo745.

Detrick, R. S., P. Buhl, E. Vera, J. Mutter, J. Orcutt, J. Madsen, and T. Brocher (1987), Multichannel seismic imaging of a crustal magma chamber along the East Pacific Rise, *Nature*, *326*(6108), 35–41, doi:10.1038/326035a0.

Dymond, J. (1981), Geochemistry of Nazca plate surface sediments–An evaluation of hydrothermal, biogenic, detrital, and hydrogenous sources, *Mem. Geol. Soc. Am.*, *154*, 133–173.

Edwards, M. H., D. J. Fornari, A. Malinverno, W. B. F. Ryan, and J. Madsen (1991), The Regional Tectonic Fabric of the East Pacific Rise From 12°50′N to 15°10′N, *J. Geophys. Res.*, *96*(B5), 7995–8017, doi:10.1029/91JB00283.

Edwards, R. L., J. W. Beck, G. S. Burr, D. J. Donahue, J. M. A. Chappell, A. L. Bloom, E. R. M. Druffel, and F. W. Taylor (1993), A large drop in atmospheric $^{14}C/^{12}C$ and reduced melting in the Younger Dryas, documented with ^{230}Th ages of corals, *Science*, *260*(5110), 962–968, doi:10.1126/science.260.5110.962.

Fairbanks, R. G., R. A. Mortlock, T. C. Chiu, L. Cao, A. Kaplan, T. P. Guilderson, T. W. Fairbanks, A. L. Bloom, P. M. Grootes, and M. J. Nadeau (2005), Radiocarbon calibration curve spanning 0 to 50,000 years BP based on paired $^{230}Th/^{234}U/^{238}U$ and ^{14}C dates on pristine corals, *Quat. Sci. Rev.*, *24*(16–17), 1781–1796, doi:10.1016/j.quascirev.2005.04.007.

Forsyth, D. W. (1992), *Geophysical Constraints on Mantle Flow and Melt Generation Beneath Mid-Ocean Ridges*, *Geophys. Monogr. Ser.*, vol. 71, AGU, Washington, D. C.

Forsyth, D. W., et al. (1998), Imaging the deep seismic structure beneath a mid-ocean ridge: The MELT experiment, *Science*, *280*(5367), 1215–1218, doi:10.1126/science.280.5367.1215.

Francois, R., M. Frank, M. M. R. van der Loeff, and M. P. Bacon (2004), ^{230}Th normalization: An essential tool for interpreting sedimentary fluxes during the late Quaternary, *Paleoceanography*, *19*, PA1018, doi:10.1029/2003PA000939.

Francois, R., et al. (2007), Comment on "Do geochemical estimates of sediment focusing pass the sediment test in the equatorial Pacific?" by M. Lyle et al, *Paleoceanography*, *22*, PA1216, doi:10.1029/2005PA001235.

Frank, M., J. D. Eckhardt, A. Eisenhauer, P. W. Kubik, B. Dittrichhannen, M. Segl, and A. Mangini (1994), Beryllium 10, thorium 230, and protactinium 231 in Galapagos microplate sediments: Implications of hydrothermal activity and paleoproductivity changes during the last 100,000 years, *Paleoceanography*, *9*(4), 559–578, doi:10.1029/94PA01132.

Froelich, P. N., G. P. Klinkhammer, M. L. Bender, N. A. Luedtke, G. R. Heath, D. Cullen, P. Dauphin, D. Hammond, B. Hartman, and V. Maynard (1979), Early oxidation of organic-matter in pelagic sediments of the eastern equatorial Atlantic: Suboxic diagenesis, *Geochim. Cosmochim. Acta*, *43*(7), 1075–1090, doi:10.1016/0016-7037(79)90095-4.

German, C. R., G. P. Klinkhammer, J. M. Edmond, A. Mitra, and H. Elderfield (1990), Hydrothermal scavenging of rare-earth elements in the ocean, *Nature*, *345*(6275), 516–518, doi:10.1038/345516a0.

German, C. R., A. C. Campbell, and J. M. Edmond (1991a), Hydrothermal scavenging at the Mid-Atlantic Ridge: Modification of trace-element dissolved fluxes, *Earth Planet. Sci. Lett.*, *107*(1), 101–114, doi:10.1016/0012-821X(91)90047-L.

German, C. R., A. P. Fleer, M. P. Bacon, and J. M. Edmond (1991b), Hydrothermal scavenging at the Mid-Atlantic Ridge: Radionuclide distributions, *Earth Planet. Sci. Lett.*, *105*(1–3), 170–181, doi:10.1016/0012-821X(91)90128-5.

German, C. R., N. C. Higgs, J. Thomson, R. Mills, H. Elderfield, J. Blusztajn, A. P. Fleer, and M. P. Bacon (1993), A geochemical study of metalliferous sediment from the TAG hydrothermal mound, 26°08′N, Mid-Atlantic Ridge, *J. Geophys. Res.*, *98*(B6), 9683–9692, doi:10.1029/92JB01705.

German, C. R., et al. (1997), Hydrothermal scavenging on the Juan de Fuca Ridge: $^{23O}Th_{xs}$, ^{10}Be, and REEs in ridge-flank sediments, *Geochim. Cosmochim. Acta*, *61*(19), 4067–4078, doi:10.1016/S0016-7037(97)00230-5.

German, C. R., J. Hergt, M. R. Palmer, and J. M. Edmond (1999), Geochemistry of a hydrothermal sediment core from the OBS vent-field, 21°N East Pacific Rise, *Chem. Geol.*, *155*(1–2), 65–75, doi:10.1016/S0009-2541(98)00141-7.

German, C. R., S. Colley, M. R. Palmer, A. Khripounoff, and G. P. Klinkhammer (2002), Hydrothermal plume-particle fluxes at 13°N on the East Pacific Rise, *Deep Sea Res., Part I*, *49*(11), 1921–1940, doi:10.1016/S0967-0637(02)00086-9.

Ghiorso, M. S., M. M. Hirschmann, P. W. Reiners, and V. C. Kress (2002), The pMELTS: A revision of MELTS for improved calculation of phase relations and major element partitioning related to partial melting of the mantle to 3 GPa, *Geochem. Geophys. Geosyst.*, *3*(5), 1030, doi:10.1029/2001GC000217.

Heath, R. S., and J. Dymond (1977), Genesis and transformation of metalliferous sediments from the East Pacific Rise, Bauer Deep and Central Basin, northwest Nazca Plate, *Geol. Soc. Am. Bull.*, *88*, 723–733, doi:10.1130/0016-7606(1977)88<723:GATOMS>2.0.CO;2.

Hung, S. H., D. W. Forsyth, and D. R. Toomey (2000), Can a narrow, melt-rich, low-velocity zone of mantle upwelling be hidden beneath the East Pacific Rise? Limits from waveform modeling and the MELT Experiment, *J. Geophys. Res.*, *105*(B4), 7945–7960, doi:10.1029/1999JB900316.

Huybers, P., and C. Langmuir (2009), Feedback between deglaciation, volcanism, and atmospheric CO2, *Earth Planet. Sci. Lett.*, *286*(3–4), 479–491, doi:10.1016/j.epsl.2009.07.014.

Jull, M., and D. McKenzie (1996), The effect of deglaciation on mantle melting beneath Iceland, *J. Geophys. Res.*, *101*(B10), 21,815–21,828, doi:10.1029/96JB01308.

Kadko, D. (1980), ^{230}Th,^{226}Ra and ^{222}Rn in abyssal sediments, *Earth Planet. Sci. Lett.*, *49*(2), 360–380, doi:10.1016/0012-821X(80)90079-5.

Kelemen, P. B., G. Hirth, N. Shimizu, M. Spiegelman, and H. J. B. Dick (1997), A review of melt migration processes in the adiabatically upwelling mantle beneath oceanic spreading ridges, *Philos. Trans. R. Soc. London, Ser. A*, *355*, 283–318, doi:10.1098/rsta.1997.0010.

Kent, G. M., A. J. Harding, and J. A. Orcutt (1990), Evidence for a smaller magma chamber beneath the east pacific rise at 9°30′ N, *Nature*, *344*(6267), 650–653, doi:10.1038/344650a0.

Kienast, S. S., M. Kienast, A. C. Mix, S. E. Calvert, and R. Francois (2007), ^{230}Th normalized particle flux and sediment focusing in the Panama Basin region during the last 30,000 years, *Paleoceanography*, *22*, PA2213, doi:10.1029/2006PA001357.

Langmuir, C. H., E. M. Klein, and T. Plank (1992), Petrological systematics of mid-ocean ridge basalts: Constraints on melt generation beneath ocean ridges, in *Mantle Flow and Melt Generation at Mid-Ocean Ridges*, *Geophys. Monogr. Ser.*, vol. 71, edited by J. P. Morgan, D. K. Blackman, and J. M. Sinton, pp. 183–280, AGU, Washington, D. C., doi:10.1029/GM071p0183.

Lisiecki, L. E., and M. E. Raymo (2005), A Pliocene-Pleistocene stack of 57 globally distributed benthic $\delta^{18}O$

records, *Paleoceanography*, *20*, PA1003, doi:10.1029/2004PA001071.

Lonsdale, P. (1994), Geomorphology and structural segmentation of the crest of the southern (Pacific-Antarctic) East Pacific Rise, *J. Geophys. Res.*, *99*(B3), 4683–4702, doi:10.1029/93JB02756.

Lund, D. C., A. C. Mix, and J. Southon (2011), Increased ventilation age of the deep northeast Pacific Ocean during the last deglaciation, *Nat. Geosci.*, doi:10.1038/ngeo1272, in press.

Lupton, J. (1998), Hydrothermal helium plumes in the Pacific Ocean, *J. Geophys. Res.*, *103*(C8), 15,853–15,868, doi:10.1029/98JC00146.

Lupton, J. E., E. T. Baker, and G. J. Massoth (1999), Helium, heat, and the generation of hydrothermal event plumes at mid-ocean ridges, *Earth Planet. Sci. Lett.*, *171*(3), 343–350, doi:10.1016/S0012-821X(99)00149-1.

Lyle, M., N. Pisias, A. Paytan, J. I. Martinez, and A. Mix (2007), Reply to comment by R. Francois et al. on "Do geochemical estimates of sediment focusing pass the sediment test in the equatorial Pacific?": Further explorations of ^{230}Th normalization, *Paleoceanography*, *22*, PA1217, doi:10.1029/2006PA001373.

Macdonald, K. C. (1982), Mid-ocean ridges: Fine scale tectonic, volcanic and hydrothermal processes within the plate boundary zone, *Annu. Rev. Earth Planet. Sci.*, *10*, 155–190, doi:10.1146/annurev.ea.10.050182.001103.

Macdonald, K. C., P. J. Fox, R. T. Alexander, R. Pockalny, and P. Gente (1996), Volcanic growth faults and the origin of Pacific abyssal hills, *Nature*, *380*(6570), 125–129, doi:10.1038/380125a0.

Maclennan, J., M. Jull, D. McKenzie, L. Slater, and K. Gronvold (2002), The link between volcanism and deglaciation in Iceland, *Geochem. Geophys. Geosyst.*, *3*(11), 1062, doi:10.1029/2001GC000282.

Marchitto, T. M., S. J. Lehman, J. D. Ortiz, J. Fluckiger, and A. van Geen (2007), Marine radiocarbon evidence for the mechanism of deglacial atmospheric CO_2 rise, *Science*, *316*(5830), 1456–1459, doi:10.1126/science.1138679.

McKenzie, D., and M. J. Bickle (1988), The volume and composition of melt generated by extension of the lithosphere, *J. Petrol.*, *29*, 625–679.

Murton, B. J., E. T. Baker, C. M. Sands, and C. R. German (2006), Detection of an unusually large hydrothermal event plume above the slow-spreading Carlsberg Ridge: NW Indian Ocean, *Geophys. Res. Lett.*, *33*, L10608, doi:10.1029/2006GL026048.

Oxburgh, R. (1998), Variations in the osmium isotope composition of sea water over the past 200,000 years, *Sci. Lett. Earth Planet*, *159*, 183–191.

Oxburgh, R. (2001), Residence time of osmium in the oceans, *Geochem. Geophys. Geosyst.*, *2*(6), 1018, doi:10.1029/2000GC000104.

Oxburgh, R., A. C. Pierson-Wickmann, L. Reisberg, and S. Hemming (2007), Climate-correlated variations in seawater ^{187}Os/^{188}Os over the past 200,000 yr: Evidence from the Cariaco Basin, Venezuela, *Earth Planet. Sci. Lett.*, *263*(3–4), 246–258, doi:10.1016/j.epsl.2007.08.033.

Perfit, M. R., and W. W. Chadwick (1998), Magmatism at mid-ocean ridges: Constraints from volcanological and geochemical investigations, in *Faulting and Magmatism at Mid-Ocean Ridges*, edited by W. R. Buck et al., pp. 59–115, AGU, Washington, D. C., doi:10.1029/GM106p0059.

Peucker-Ehrenbrink, B., and G. Ravizza (2000), The marine osmium isotope record, *Terra Nova*, *12*(5), 205–219, doi:10.1046/j.1365-3121.2000.00295.x.

Pineau, F., and M. Javoy (1994), Strong degassing at ridge crests: The behaviour of dissolved carbon and water in basalt glasses at 14°N, Mid-Atlantic Ridge, *Earth Planet. Sci. Lett.*, *123*(1–3), 179–198, doi:10.1016/0012-821X(94)90266-6.

Proskurowski, G., M. D. Lilley, and T. A. Brown (2004), Isotopic evidence of magmatism and seawater bicarbonate removal at the endeavour hydrothermal system, *Earth Planet. Sci. Lett.*, *225*(1–2), 53–61, doi:10.1016/j.epsl.2004.06.007.

Richardson, C., and D. McKenzie (1994), Radioactive disequilibria from 2D models of melt generation by plumes and ridges, *Earth Planet. Sci. Lett.*, *128*, 425–437, doi:10.1016/0012-821X(94)90160-0.

Rose, K. A., E. L. Sikes, T. P. Guilderson, P. Shane, T. M. Hill, R. Zahn, and H. J. Spero (2010), Upper-ocean-to-atmosphere radiocarbon offsets imply fast deglacial carbon dioxide release, *Nature*, *466*(7310), 1093–1097, doi:10.1038/nature09288.

Rubin, K. H., I. van der Zander, M. C. Smith, and E. C. Bergmanis (2005), Minimum speed limit for ocean ridge magmatism from ^{210}Pb–^{226}Ra–^{230}Th disequilibria, *Nature*, *437*(7058), 534–538, doi:10.1038/nature03993.

Ruhlin, D. E., and R. M. Owen (1986), The rare-earth element geochemistry of hydrothermal sediments from the east pacific rise: Examination of a seawater scavenging mechanism, *Geochim. Cosmochim. Acta*, *50*(3), 393–400, doi:10.1016/0016-7037(86)90192-4.

Scott, D. R., and D. J. Stevenson (1989), A self-consistent model of melting, magma migration and buoyancy-driven circulation beneath mid-ocean ridges, *J. Geophys. Res.*, *94*(B3), 2973–2988, doi:10.1029/JB094iB03p02973.

Sharma, M., G. J. Wasserburg, A. W. Hofmann, and D. A. Butterfield (2000), Osmium isotopes in hydrothermal fluids from the Juan de Fuca Ridge, *Earth Planet. Sci. Lett.*, *179*(1), 139–152, doi:10.1016/S0012-821X(00)00099-6.

Sharma, M., E. J. Rosenberg, and D. A. Butterfield (2007), Search for the proverbial mantle osmium sources to the oceans: Hydrothermal alteration of mid-ocean ridge basalt, *Geochim. Cosmochim. Acta*, *71*(19), 4655–4667, doi:10.1016/j.gca.2007.06.062.

Sortor, R. N., and D. C. Lund (2011), No evidence for a deglacial intermediate water Δ^{14}C anomaly in the SW Atlantic, *Earth Planet. Sci. Lett.*, *310*, 65–72, doi:10.1016/j.epsl.2011.07.017.

Speer, K. G., M. E. Maltrud, and A. M. Thurnherr (2003), A global view of dispersion above the mid-ocean ridge, in *Energy and Mass Transfer in Hydrothermal Systems*, edited by P. E. Halbach, V. Tunnicliffe, and J. R. Hein, pp. 287–302, Dahlem Univ. Press, Berlin.

Spiegelman, M. (1993a), Flow in deformable porous media. Part 1: Simple analysis, *J. Fluid Mech.*, *247*, 17–38, doi:10.1017/S0022112093000369.

Spiegelman, M. (1993b), Flow in deformable porous media. Part 2: Numerical analysis–the relationship between shock waves and solitary waves, *J. Fluid Mech.*, *247*, 39–63, doi:10.1017/S0022112093000370.

Spiegelman, M. (1996), Geochemical consequences of melt transport in 2-D: The sensitivity of trace elements to mantle, *Earth Planet. Sci. Lett.*, *139*(1–2), 115–132, doi:10.1016/0012-821X(96)00008-8.

Spiegelman, M., and T. Elliott (1993), Consequences of melt transport for uranium series disequilibrium in young lavas, *Earth Planet. Sci. Lett.*, *118*, 1–20, doi:10.1016/0012-821X(93)90155-3.

Spiegelman, M., and D. McKenzie (1987), Simple 2-D models for melt extraction at mid-ocean ridges and island arcs, *Earth*

Planet. Sci. Lett., *83*(1–4), 137–152, doi:10.1016/0012-821X(87)90057-4.

Stott, L., J. Southon, A. Timmermann, and A. Koutavas (2009), Radiocarbon age anomaly at intermediate water depth in the Pacific Ocean during the last deglaciation, *Paleoceanography*, *24*, PA2223, doi:10.1029/2008PA001690.

Thompson, W. G., and S. L. Goldstein (2006), A radiometric calibration of the SPECMAP timescale, *Quat. Sci. Rev.*, *25*(23–24), 3207–3215, doi:10.1016/j.quascirev.2006.02.007.

Thornalley, D. J. R., S. Barker, W. S. Broecker, H. Elderfield, and I. N. McCave (2011), The deglacial evolution of North Atlantic deep convection, *Science*, *331*(6014), 202–205, doi:10.1126/science.1196812.

Toner, B. M., S. C. Fakra, S. J. Manganini, C. M. Santelli, M. A. Marcus, J. Moffett, O. Rouxel, C. R. German, and K. J. Edwards (2009), Preservation of iron(II) by carbon-rich matrices in a hydrothermal plume, *Nat. Geosci.*, *2*(3), 197–201, doi:10.1038/ngeo433.

Turcotte, D. L., and J. P. Morgan (1992), *The Physics of Magma Migration and Mantle Flow Beneath a Mid-Ocean Ridge*, *Geophys. Monogr. Ser.*, vol. 71, 361 pp., AGU, Washington, D. C., doi:10.1029/GM071.

Williams, G. A., and K. K. Turekian (2004), The glacial-interglacial variation of seawater osmium isotopes as recorded in Santa Barbara Basin, *Earth Planet. Sci. Lett.*, *228*(3–4), 379–389, doi:10.1016/j.epsl.2004.10.004.

Workman, R. K., and S. R. Hart (2005), Major and trace element composition of the depleted MORB mantle (DMM), *Earth Planet. Sci. Lett.*, *231*(1–2), 53–72, doi:10.1016/j.epsl.2004.12.005.

Yang, Y. L., H. Elderfield, T. F. Pedersen, and M. Ivanovich (1995), Geochemical record of the panama basin during the last glacial maximum carbon event shows that the glacial ocean was not suboxic, *Geology*, *23*(12), 1115–1118, doi:10.1130/0091-7613(1995)023<1115:GROTPB>2.3.CO;2.

Yu, E. F., R. Francois, M. P. Bacon, and A. P. Fleer (2001), Fluxes of ^{230}Th and ^{231}Pa to the deep sea: Implications for the interpretation of excess ^{230}Th and ^{231}Pa/^{230}Th profiles in sediments, *Earth Planet. Sci. Lett.*, *191*(3–4), 219–230, doi:10.1016/S0012-821X(01)00410-1.